THESIS

LATENT HEATING AND CLOUD PROCESSES IN WARM FRONTS

Submitted by

Adele Igel

Department of Atmospheric Science

In partial fulfillment of the requirements

For the Degree of Master of Science

Colorado State University

Fort Collins, Colorado

Fall 2012

Master's Committee:

Advisor: Susan van den Heever

Steven Rutledge
Karan Venayagamoorthy

ABSTRACT

LATENT HEATING AND CLOUD PROCESSES IN WARM FRONTS

The results of two studies are presented in this thesis. In the first, an extratropical cyclone that crossed the United States on April 9-11 2009 was successfully simulated at high resolution (3km horizontal grid spacing) using the Colorado State University Regional Atmospheric Modeling System. The sensitivity of the associated warm front to increasing pollution levels was then explored by conducting the same experiment with three different background profiles of cloud-nucleating aerosol concentration. To our knowledge, no study has examined the indirect effects of aerosols on warm fronts. First the budgets of ice, cloud water, and rain in the simulation with the lowest aerosol concentrations were examined. The ice mass was found to be produced in equal amounts through vapor deposition and riming and the melting of ice produced ~75% of the total rain. Conversion of cloud water to rain accounted for the other 25%. When cloud-nucleating aerosol concentrations were increased, significant changes were seen in the budget terms, but total precipitation was relatively constant. Vapor deposition onto ice increased, but riming of cloud water decreased such that there was only a small change in the total ice production and hence there was no significant change in melting. These responses can be understood in terms of a buffering effect in which smaller cloud droplets in the mixed phase region lead to both an enhanced Bergeron process and decreased riming efficiencies with increasing aerosol concentrations. Overall, while large changes were seen in the microphysical structure of the frontal cloud, cloud-nucleating aerosols had little impact on the precipitation production of the warm front.

The second study addresses the role of latent heating associated with the warm front by assessing the relative contributions of individual cloud processes to latent heating and frontogenesis in both the horizontal and vertical directions. Condensation and cloud droplet nucleation are the largest sources of latent heat along the frontal surface and together produce rates of horizontal frontogenesis that are of the same order of magnitude as the deformation and tilting terms at midlevels; however near the surface latent heating does not cause strong frontogenesis. In the vertical, frontogenesis caused by these two processes is nearly everywhere higher than frontogenesis caused by dry dynamics, and are the primary mechanisms through which high static stability is found along the frontal surface. The horizontal and vertical components of frontogenesis are combined in a new way to form an expression for the frontal slope tendency. While dynamic processes lead to increases in frontal tilt, latent heating often counteracts this tendency. This indicates that the direct effect of latent heating on the thermal structure of the front is to decrease the slope and in that sense weaken the warm front.

ACKNOWLEDGEMENTS

Many people are to be thanked for making this work possible. Above all, I'd like to thank Dr. Susan van den Heever for taking me on as a student, for guiding me through this project, and for encouraging me to take advantage of conferences and fellowships. Dr. Catherine Naud developed the objective frontal detection algorithm used in both studies, and never got annoyed when, on multiple occasions, I told her the algorithm needed tweaking; without warm front locations this work really could not have been done. Thank you to Stephen Saleeby for working with me on the numerous obstacles that had to be overcome in order to successfully run RAMS and to Natalie Tourville for keeping the computers running despite my best efforts to kill the cluster. Susan van den Heever, Catherine Naud, Stephen Saleeby, and Dr. Derek Posselt are all coauthors on the first manuscript presented in this thesis; thank you all for your helpful comments and suggestions. Susan van den Heever is also a coauthor on the second manuscript. I am also grateful to Drs. Steven Rutledge and Karan Venayagamoorthy for serving on my committee. Thank you to the van den Heever group for their help in solving daily problems and for making every day fun. And last but not least, thank you to Matt Igel for his discussions about the nature of latent heating and clouds.

This work has been supported by an AMS graduate scholarship and NASA grant NNX10AM20G.

TABLE OF CONTENTS

I. Introduction

Extratropical cyclones (ETCs) have been studied for nearly a century. Bjerknes first published a paper on extratropical cyclones in 1919 in which he identified the warm and cold fronts as the steering and squall lines, respectively. In 1922, Bjerknes and Solberg published another paper that described the evolution of the extratropical cyclone and its fronts. The ideas that he and his contemporaries put forward are known today as the Norwegian Cyclone Model (NCM) and it is remarkable how little it has changed in the intervening hundred years.

In this work the focus is on the warm front. In the Norwegian Cyclone Model, warm fronts are depicted as gently sloping surfaces that separate relatively warm and cool air masses. The warm air retreats as the cold air pushes up and over the front. Clouds are found along this surface such that cloud tops and bases lower as one approaches the surface position of the front. Precipitation intensity smoothly increases as the surface front approaches a given location. Winds veer with height, which is consistent with warm air advection according to the thermal wind relation and stable lapse rates are found within the frontal zone. The warm front extends from the cyclone center but moves more slowly than the cold front. Eventually the cold front "catches up" with the warm front to form an occlusion. While many of these features still define a warm front today, some modifications have been made and further insights gained.

Aircraft, radar, and satellite observations have provided unprecedented insight into the structure of fronts. It has been found that cloud top height varies little with frontal position and that low-level clouds are found both before and after the warm frontal passage (Posselt et al., 2008; Naud et al., 2011), which is not in keeping with the classic NCM picture of warm fronts. There has also been a modification to the NCM idea that warm fronts are gently sloping surfaces. Observations have found areas in which the front is in fact steeply sloped and others in which it

is nearly horizontal (Locatelli and Hobbs, 1987). This kind of structure was also seen by Neiman et al. (1993) and they termed it the "escalator-elevator" concept of airflow over a warm front. This refinement allows for the gentle upsloping air to be punctuated by areas of mesoscale convection. These areas of convection can produce heavier precipitation and hence also calls into question the picture of uniform precipitation that slowly decreases in intensity away from the surface front in the NCM. The locally heavy precipitation is often organized into bands (Hobbs, 1978; Houze et al., 1976; Hobbs and Locatelli, 1978), where these bands can be either parallel or perpendicular to the warm front (Hudak et al., 1996). Latent heating has been found necessary for banded structures in vertical velocity (Knight and Hobbs, 1988) and rainfall, but their formation mechanisms are not fully understood. Rain bands may form through the release of symmetric instability and are often associated with gravity or Kelvin-Helmholtz waves (Wakimoto et al., 1992; Hudak et al., 1996; Hogan et al., 2002). The seeder-feeder mechanism has been shown in radar and modeling studies to intensify the precipitation in these warm frontal rain bands (Herzegh and Hobbs, 1980; Houze et al., 1981; Rutledge and Hobbs, 1983).

More significantly, a second basic configuration of the cold and warm fronts has been identified in which the cold front advances away from the cyclone's center while the warm front extends into the northwest quadrant of the storm. This is known as a "bent-back" warm front and the "t-bone" configuration of the two fronts is found to occur primarily over oceans (Shapiro and Keyser, 1990). The structure was particularly well documented during the ERICA field campaign (Wakimoto et al., 1992, 1995; Blier and Wakimoto, 1995). These studies demonstrated that the extension of the front did not resemble the structure of an occluded front, but rather the structure of a warm front. It was unclear as to whether the bent-back front was a result of advection of the warm front westward relative to the cyclone center, or whether it

developed through local deformation and convergence of the wind field. The fact that bent-back warm fronts are most commonly seen associated with maritime ETCs is perhaps due to low surface drag over oceans (Hines and Mechoso, 1993), though similar structures have been observed with ETCs occurring over land, even if less frequently (Martin, 1998).

Finally, the conveyor belt conceptual model of extratropical cyclones (Carlson, 1980; Browning and Roberts, 1994) has been introduced that identifies the major airstreams in extratropical cyclones. The most prominent of these are the warm conveyor belt (Harrold, 1973), a warm, moist poleward flow of air ahead of the cold front that rises over the warm front, and the cold conveyor belt (Carlson, 1980), a cool, dry flow of air beneath the warm front that wraps around the storm center. The warm conveyor belt can bifurcate aloft with one part turning anticyclonically and another cyclonically (Mass and Schultz, 1993). The anticyclonic branch flows into the upper-level ridge, while the cyclonic branch helps to form a trough of warm air aloft called the trowal (Martin, 1998). (what about the dry conveyor belt? Or the dry air stream?)

One aspect of warm (and cold) fronts not addressed by the NCM is their formation mechanisms and theoretical explanations for their circulations. It has been found that a sloping boundary between air masses of different densities is insufficient to explain the rising air found along frontal surfaces. Rather, it is the confluence of wind in the presence of these boundaries leading to increases in the temperature gradient, and an imbalance in the thermal wind, that gives rise to the vertical motions as discussed by Sawyer (1956). Work by Eliassen (1962) extended the concepts of Sawyer (1956) to develop a semigeostrophic theoretical framework through which the transverse circulations in frontal zones can be understood. Semigeostrophic theory differs from the more familiar quasigeostrophic theory in that the advecting wind is the full wind

rather than the geostrophic wind. Today the equation describing the circulation in frontal zones is known as the Sawyer-Eliassen transverse circulation equation.

The frontogenesis equation, an equation describing the evolution of potential temperature gradients and first introduced by Petterssen (1936), has also provided insight into the formation of fronts. Potential temperature gradients can be changed through horizontal deformation or horizontal shearing of the thermal field or through their vertical tilting and stretching. Gradients in diabatic heating can also influence the potential temperature gradients. Some observational studies have tried to quantify the relative contributions of each of the frontogenetic processes in warm fronts. Riordan (1990) estimated that confluence at the surface is very large and must be counteracted by differential diabatic processes. Hanesiak et al. (2007) found horizontal confluence to be frontogenetic everywhere along the frontal surface, but that locally tilting dominated the frontogenesis. Surface drag has been observed to significantly slow the movement of warm fronts (Kemppi and Sinclair, 2011).

In general it is difficult to calculate frontogenesis from observations since a high-resolution data set is needed in order to accurately estimate the many spatial derivatives that are involved. As a result, most studies of frontogenesis use a modeling approach. Frontogenesis has been extensively studied through idealized, dry semigeostrophic models (Davies, 1994 and references therein). While these studies have been successful in explaining the basic dynamics of front formation, it is often seen that these models cannot reproduce the observed vertical velocities found at fronts. This points to the important role of diabatic effects in fully explaining the structure of fronts. Many modeling studies have shown that latent heating through cloud condensation and other microphysical processes does in fact greatly increase vertical velocities and narrows the region of ascent at fronts (Thorpe and Emanuel, 1985; Chan and Cho, 1991; Han

et al., 2007). In addition, significant positive (negative) potential vorticity anomalies can be created below (above) the region of maximum heating. These can alter the horizontal wind fields and strengthen the ageostrophic circulation leading to enhanced moisture convergence and enhanced frontogenesis (Mak and Bannon, 1984; Chan and Cho, 1991). The potential vorticity anomalies due to latent heating associated with the warm front in particular are thought to be important for the formation of the occlusion (Posselt and Martin, 2004), upper-level ridge building (Ahmadi-Givi et al., 2004), and explosively deepening cyclones (Whitaker and Davis, 1993). Clearly latent heating is important in the dynamics of warm fronts and in the distribution of precipitation associated with them.

This is a two-part thesis in which the latent heating by warm fronts is explored. In chapter II, the idea that latent heating associated with warm fronts can be modified significantly by different ambient cloud-nucleating aerosol concentrations, leading to changes in warm frontal structure and precipitation, is explored. In chapter III, efforts are made to further understand the role of latent heating in modifying the thermal structure of warm fronts through a novel use of the frontogenesis equations. Chapters II and III are manuscripts that have been accepted for publication to the *Journal of Atmospheric Science* and the *Quarterly Journal of the Royal Meteorological Society*, respectively.

II. Sensitivity of warm frontal processes to cloud-nucleating aerosol concentrations

2.1. Introduction

The indirect effects of aerosols on cloud systems cause a large uncertainty when trying to predict future climate (IPCC, 2007). Much effort has gone in to studying the impacts of aerosols on deep convection, trade wind cumulus, stratocumulus decks, and orographic clouds (Khain, 2009; Tao, et al., 2012, and references therein). However, to our knowledge, no study has looked at the indirect effect of aerosols on extratropical cyclones, despite the fact that both changes in pollution emissions globally and local seasonal enhancements of aerosol concentrations due to burning (Wang et al., 2009) could impact these systems.

Extratropical cyclones are the primary transporters of moisture, heat, and energy poleward in the midlatitudes (e.g. Trenberth and Stepaniak, 2003, Schneider et al., 2006). The fronts associated with extratropical cyclones contribute ~68% of the total precipitation at midlatitudes (Catto et al., 2012). Additionally their deep and extensive cloud shields have large impacts for radiation locally and on climate scales (e.g. Ramanathan et al., 1989). Should aerosols be able to alter the radiative, microphysical, and/or dynamical properties of extratropical cyclones, they could have important consequences for global change scenarios.

Aerosols can impact cloud systems such as extratropical cyclones through direct absorption, reflection, or scattering of radiation, or by changing the microphysical structure of clouds. A change in cloud microphysical structure can affect the radiative properties of clouds (Twomey, 1977), change the lifetime of clouds (Albrecht, 1989), or alter the rates of microphysical processes associated with latent heat release. Changes in radiative and latent heating rates can then induce changes in vertical velocities and other dynamical fields. Understanding all of these indirect effects and feedbacks of aerosols is an ongoing and difficult

task, especially since the environment and dynamics of the system itself can alter the response to aerosols (Matsui et al., 2006; Fan et al., 2009; Khain, 2009; Storer et al., 2010). Since the mesoscale dynamics of an extratropical cyclone differ greatly between the cold and warm fronts, a detailed study of all of the impacts of aerosols on extratropical cyclones is too extensive for one study; therefore, this paper will focus on just one part of the extratropical cyclone, the warm front.

While there are no studies that specifically examine the influence of aerosols on extratropical cyclones, research has been conducted on the impact of latent heating on these systems. On a storm wide scale, strong latent heating can have significant contributions to upper- and lower-level potential vorticity anomalies and is often associated with the most intense and rapidly developing systems (Čampa and Wernli, 2012). In some case studies, latent heating has been found to simply augment the dry dynamics (e.g. Davis et al., 1993), whereas in others it has been the primary contributor to storm intensity (e.g Stoelinga, et al., 1996). More specifically, latent heat release has been found to be critical in building the warm occluded structure associated with the classic treble clef in upper level potential vorticity (Posselt and Martin, 2004) as well as in helping to build the downstream ridge (Pomroy and Thorpe, 2000; Ahmadi-Givi et al., 2004; Grams et al., 2011).

On the frontal scale, latent heating is thought to play a role in many ways. First, modeling studies have shown that latent heat processes, including condensation and melting, lead to mesoscale banded features over the warm frontal surface (Hsie et al., 1984; Szeto and Stewart, 1997). Evaporational and sublimational cooling can enhance regions of mesoscale descent (Huang and Emanuel, 1990; Clough et al., 2000). Through these modifications of vertical velocity and circulation as well as through local changes in the thermal structure, latent heating

has been seen to accelerate frontogenesis and frontal propagation speed for both warm and cold fronts (Hsie et al., 1984; Szeto and Stewart, 1997; Reeves and Lackmann, 2004). It is difficult to predict what the aerosol-induced changes to cloud structure and precipitation will be due to the many competing interactions at play in the warm front from the micro- to synoptic scales. Therefore it is unknown whether or not the changes that do occur will be sufficient to alter latent heat release such that any of the impacts of latent heating discussed above can be realized in actual storms. This study seeks to explore these previously unaddressed concerns associated with the warm front.

Before the impacts of aerosols on warm fronts can be fully understood, the budgets of ice and liquid hydrometeor mass must be examined since aerosol indirect effects vary with cloud phase. Such budgets of cloud ice and rain, but not cloud liquid, have been studied before by Rutledge and Hobbs (1983) and Gedzelman and Arnold (1993) for warm fronts; however, both of those studies used idealized, two-dimensional model setups with more primitive microphysical schemes than is used in the present study. The current work will expand on these previous studies by presenting budgets of ice, rain, and for the first time cloud liquid from a three-dimensional, high resolution cloud-resolving simulation of a case study that employs a sophisticated microphysics parameterization. The sensitivity of the budgets and latent heating profiles of the warm front will then be tested by altering the background profile of cloud-nucleating aerosol concentration in two additional simulations.

In section 2, the model will be described and a synoptic overview of the selected storm given. In section 3, data analysis methods will be described. Section 4 includes the budgets of ice, cloud liquid, and rain, in warm frontal clouds. In section 5 the sensitivity of these budgets and the warm front as a whole to perturbations in aerosol concentrations is discussed.

2.2. Case Overview

2.2.1. Case selection and model setup

To approach this problem, an extratropical cyclone was simulated using the Regional Atmospheric Modeling System (RAMS) (Pielke et al., 1992; Cotton et al., 2003). The case selected was the extratropical cyclone that developed in the lee of the Rocky Mountains and tracked across the United States from 9-11 April 2009. This case was selected for several reasons. Most importantly, it had a long-lived and well-defined warm front. Additionally no other extratropical cyclone was near enough to interact with this one, which would further complicate the analysis. Thirdly, the case was chosen because it did not move from water to land or vice versa until after the simulation period. In this way transitions between water and land surfaces do not complicate interpretation of the results. Finally, the satellite-borne cloud radar onboard CloudSat (Stephens et al., 2002) overpassed the warm front twice and provided an observational constraint to evaluate the model accuracy.

The simulations were set up with an outer and inner two-way nested grid, the locations of which are shown in Figure 2.1a. The outer grid has 250x300 grid points with 15km horizontal spacing while the inner grid has 697x1027 grid points with 3km horizontal spacing. To our knowledge, no extratropical cyclone has been simulated at this grid resolution before. Both grids have 45 vertical sigma levels, with 75m spacing near the surface stretching to 1km spacing at the model top. The time steps on the inner and outer grids were 5 and 20s, respectively. A cumulus parameterization scheme based on Kuo (1974) and Molinari (1985) was implemented on the outer grid only. The Harrington (1997) radiation scheme and a Smagorinsky (1963) turbulence scheme with modifications by Lilly (1962) and Hill (1974) were implemented on both grids.

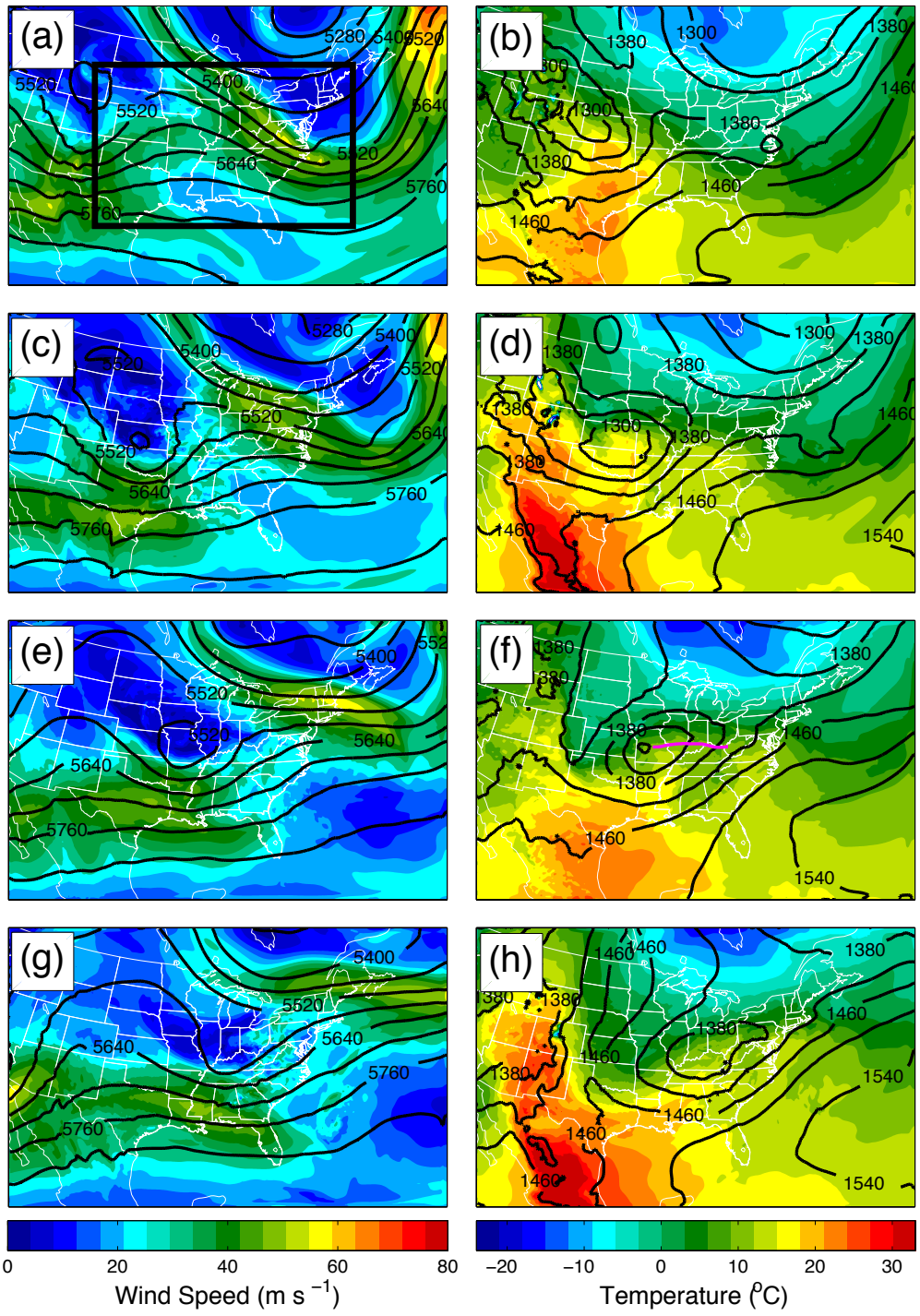

Fig. 2.1. (a), (c), (e), (g) 300mb wind speed (shaded) and, 500mb geopotential height (contoured) and (b), (d), (f), (h) 850mb temperature (shaded) and geopotential height (contoured) output from the outer grid at (a-b) 12 UTC 9 April, (c-d) 00 UTC 10 April, (e-f) 12 UTC 10 April, and (g-h) 00 UTC 11 April. The heavy pink line in (f) is the objective location of the warm front.

The simulations use a two-moment bin-emulating microphysical scheme (Saleeby and Cotton, 2004, 2007) that includes five prognostic ice species: pristine ice, snow, aggregates, graupel, and hail, and three prognostic liquid species: two cloud droplet modes (Saleeby and Cotton, 2004) and rain. By using a bin-emulating scheme, each species is binned by size for the calculation of collection efficiencies and fall speeds which gives a more accurate representation of riming and autoconversion than can be simulated by using a bulk microphysics scheme. This parameterization scheme is therefore well suited for the study of the microphysics and precipitation of the warm front without being too memory intensive.

RAMS explicitly tracks the rates of many cloud processes. Those that will be presented here (the names used in the figures are given in parentheses) are total vapor deposition and sublimation of ice species (vapor to ice), total condensation and evaporation of cloud species (vapor to cloud) and rain (vapor to rain), cloud droplet nucleation (cloud nucleation), conversion of cloud liquid to rain through autoconversion of cloud droplets and accretion of cloud droplets by rain (cloud to rain), melting (melting), riming of cloud droplets (riming of cloud) and raindrops (riming of rain), and collection of ice by rain resulting in the melting of the ice (ice to rain). These allow for the budgets of ice, cloud liquid, and rain to be explicitly calculated in the simulations. Note though that the two processes comprising each of the following pairs - deposition and sublimation, condensation and evaporation, and the cloud to rain processes - are not tracked separately and thus cannot be examined individually.

The model was initialized using Global Forecast System (GFS) analysis at 00 UTC 9 April 2009 and integrated for 48 hours. The lateral boundaries were nudged every 6 hours using additional GFS analyses. The profile of those aerosols that can serve as cloud condensation nuclei (CCN) was maximized at the surface and decreased linearly from the surface value up to

4km above which it was constant at 100 cm^{-3}. The model was run three times with surface aerosol concentrations of 400, 800, and 1600 cm^{-3}; these concentrations are representative of clean, average, and polluted conditions over continents (Andreae, 2009). These sensitivity runs will be referred to as CCN400, CCN800, and CCN1600, respectively. Apart from the differences in initial aerosol concentrations, the model setups were identical. The cloud-nucleating aerosol particles were allowed to be advected horizontally and vertically, but were not depleted during cloud nucleation. Additionally the aerosols were not radiatively active.

2.2.2. Synoptic overview

Figure 2.1 shows output from CCN400 depicting the evolution of the storm. At 12 UTC April 9, a broad trough exists at both 300 and 500mb over the Rocky Mountains associated with a closed low at 850mb beginning to form in eastern Colorado and western Kansas. Twelve hours later the trough at 500mb has formed a cutoff low, the downstream ridge has weakened, and the low at 850mb has deepened. There is an enhanced potential temperature gradient at 850mb extending eastward from the low center, consistent with the presence of confluent background flow (Schultz et al., 1998). This is the warm front that will be the focus of this study. There is also a narrow tongue of warm air reaching the center of the circulation from the south that could also be considered a warm front. This boundary was associated with a severe weather outbreak in the southeast on the 9th and 10th, but will not be discussed in this paper.

At 12 UTC April 10 the system is near its peak intensity. The low centers have become vertically stacked and begin to weaken shortly after this time. The warm front of interest is now associated with a distinct trough in the 850mb field and its eastern end is beginning to interact with the Appalachian Mountains. The jet streak at 300mb in the northeast has intensified but

shifted little in the horizontal and is likely aiding in large-scale lift over the warm front. By 00Z April 11 the low center is just to the west of the mountains. As it is not the objective of this study to examine the influence of the mountains on the warm front, the simulation was ended here, though the system did continue to the Atlantic Ocean and regained strength over the Gulf Stream.

2.2.3. Validation

Figure 2.2a shows the NWS radar estimated rainfall and Figure 2.2b the CCN400 total precipitation for the 24-hour period ending 12 UTC April 10. The general pattern of precipitation is well captured, especially around the warm front. RAMS correctly places the maximum in precipitation in northern Missouri and southern Illinois and Indiana, though perhaps it is shifted slightly north and east. The local maxima in RAMS are higher than those seen in the radar estimate, but the average totals of 1-4 cm seem to be consistent. RAMS does underpredict rainfall in the southeast associated with the secondary warm front, but that is not a major concern for the analysis that will be presented here.

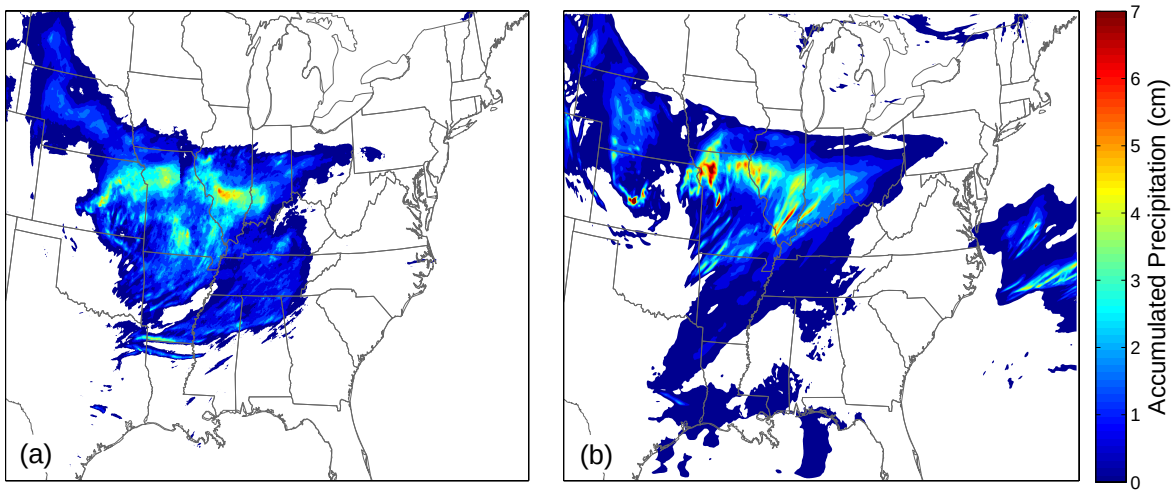

Fig. 2.2. (a) Radar derived estimate of the 24-hour precipitation total ending 12Z April 10 from the National Weather Service. (b) Precipitation total for the same time period but from RAMS output.

The structure of the warm front is also compared to two CloudSat radar reflectivity transects (Fig. 2.3). RAMS output from the inner grid for CCN400 was matched to the transect path and averaged over the hours preceeding and proceeding the CloudSat overpasses, the first of which occurred ~19:34 UTC April 9 and the second of which occurred ~18:38 UTC April 10. The model reflectivity fields shown were generated by inputting the mixing ratio and number concentration of each hydrometeor species into the radar simulator Quick-Beam (Haynes et al., 2007). In both cases the magnitude of reflectivity above 2km, the mixed-phase and ice regions of the cloud, is too low compared to observations, suggesting that ice contents are too low. However Quick-Beam does not include the effects of multiple scattering or the bright band, both of which could be contributing to the lower reflectivity seen in the model output. The pattern of reflectivity, the magnitude of reflectivity below the melting level, and cloud top height from RAMS all compare favorably with the CloudSat transects at each time. These results give confidence that the model is reproducing the overall cloud structure well.

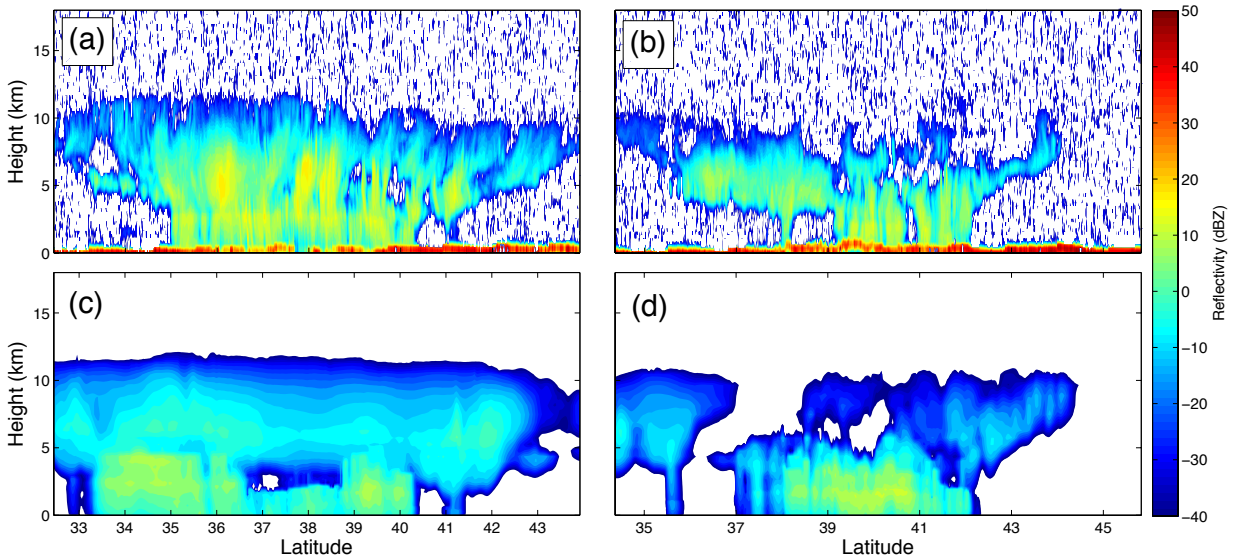

Fig. 2.3. Vertical cross sections through the warm front of (a), (b) radar reflectivity from CloudSat overpasses at 19:34 UTC 9 April and 18:38 UTC 10 April, respectively and (c), (d) corresponding RAMS reflectivity generated using Quick-Beam with data from the nearest two output files in time.

2.3. Methods

2.3.1. Warm front detection

In order to objectively locate the warm front at each hour, we used modeled temperature and pressure outputs, and applied the front detection algorithm of Hewson (1998) on equal-sigma surfaces rather than equal-pressure surfaces as in previous work (e.g. Naud et al., 2012). The latter work was performed over the oceans, while this study is over land, with large variations in surface heights. We calculated potential temperatures at the surface (θ_{surf}) for the entire domain, as well as the geostrophic wind velocity (V_{G_surf}) using the geopotential height field. While Hewson (1998) recommended using the 900 hPa level for detecting surface fronts, we found that the surface fields were much less noisy and produced cleaner results than other near-surface levels. The technique proposed by Hewson (1998) was originally conceived for fields of about 100 km horizontal resolution, but here the resolution is 3km, so we had to make several adjustments. We first subsetted θ_{surf} and V_{G_surf} every 30 km and then applied a smoothing routine (simply the average of four times the central point with its four nearest neighbors). These two fields were then fed into the front detection routine. As fully explained in Hewson (1998), the potential temperature gradient is first calculated at each point in the domain grid, then used to calculate the spatial rate of change of the gradient ($\nabla|\nabla\theta|$). Frontal boundaries are those grid points where the 'along-vector divergence' of $\nabla|\nabla\theta|$ is null. Two masks are then applied to select those that are most probably the cold and warm fronts, and finally, the sign of the product of geostrophic wind velocity and potential temperature gradient delineates between warm and cold fronts. We added another step to remove cold and warm fronts associated with neighboring cyclones, as in Naud et al. (2010). This was simply achieved by isolating the location of the deepest minimum in sea level pressure and keeping fronts within 15º of this minimum (to the

south for cold fronts and west for warm front) that had a temperature gradient greater than $25x10^{-6}$ K m^{-1}.

Despite the upscaling and smoothing, multiple warm fronts were detected, in part due to using the surface potential temperature field. In order to objectively isolate the primary front, additional masks were applied. Warm frontal points within 0.75° latitude or longitude of a coastline were removed. These points existed simply due to the large constrast in potential temperature between land and ocean and did not represent the warm front associated with the extratropical cyclone. Warm frontal points were also required to have cloud cover within 60km to the north. This condition was used to eliminate the boundary oriented north-south in the warm sector of the storm that was associated with the severe weather outbreak mentioned earlier. Finally, warm frontal points with four or fewer neighbors within 150km, one or zero neighbors within 60km, or zero neighbors within 300km in the next hour were thrown out. The effects of these conditions were to remove short-lived warm frontal structures. Finally a 10-degree polynomial was fit to the remaining warm frontal points. The effect of using the high-degree polynomial was to preserve the shape and location of the warm front while smoothing clusters of points and to recover the original 3 km inner grid resolution.

The final objective locations of the warm front at each hour (see for example the one in Figure 2.1f) show that the detection algorithm effectively locates the warm front such that it is continuous in time. It performs best from hours 28-43 of the simulation during which time almost the entire length of the front propagates forward at each time step. It is over this interval that the analyses presented here will be conducted.

2.3.2. Averaging

The objective warm front locations were used to create average cross sections through the front. The distance to the storm center and length of the front varies in time. However to maintain a consistent data volume for each time, warm fronts were defined to begin 60km east of the low pressure center and to be 573km long (the length of the shortest analyzed front in the simulation). The warm fronts are nearly parallel to the west-east direction at each time step (Fig. 2.1f, for example), so no rotation of the data was necessary. Model output was taken along a north-south transect at each grid point along the front and averaged along the east-west direction to obtain a single composite cross section perpendicular to the front at each hour. The meridional span captured the bulk of the precipitation and cloud field associated with the warm front. Figure 2.4 shows Hovmoller diagrams of the zonal wind (u) and the meridional wind (v) and potential temperature at the surface as a function of distance from the front. It can be seen that the warm front detection and averaging correctly places the front on the warm side of the baroclinic zone and that the cross front wind shifts from positive to negative as expected. This indicates that the front detection and averaging is effectively capturing the features of the front.

No minimum threshold for process rate or condensate is used in any of the averaging since cloud and/or precipitation are present in most of the subsetted domain. The exceptions are

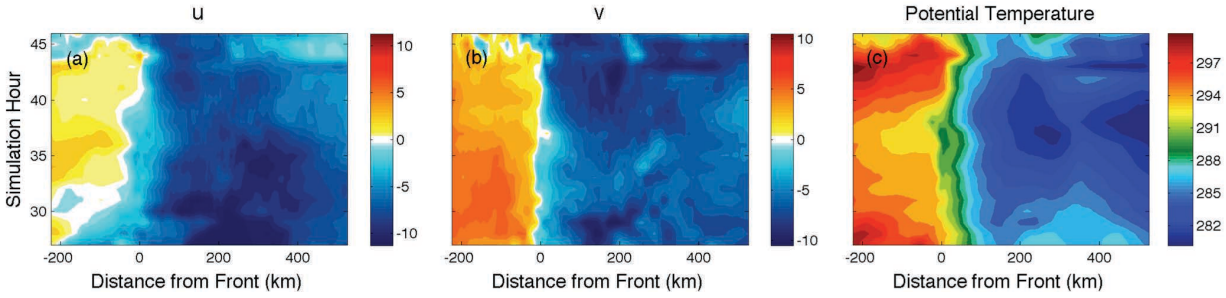

Fig. 2.4. Hovmoller diagrams of the average u, v, and potential temperature at the surface as a function of distance from the warm front.

hydrometeor diameters, which are averaged only where they are nonzero and are weighted by the number concentration of the proper species. All vertical profiles shown in the figures to follow are further averages from the front to 525km north of the front. While areas south of the front were also cloud covered and receiving precipitation, precipitation was often due to warm sector convection that is not representative of the more stratiform cloud regime dominant in this case and thus this area was not included. By averaging to 525km ahead of the front, nearly the full extent of the warm frontal cloud is captured, though at its furthest reaches, only ice exists and liquid species are not present.

2.4. Cloud Budgets

Figure 2.5 shows average vertical profiles of each of the most important processes contributing to the production or depletion of ice species, cloud liquid, and rain in CCN400. The ice budget (Fig. 2.5a) shows that vapor deposition is the dominant growth process above ~4.5km whereas riming is dominant below that level. This being a warm spring case (Fig. 2.1), very little ice reaches the surface in the simulation and therefore most ice that is produced must

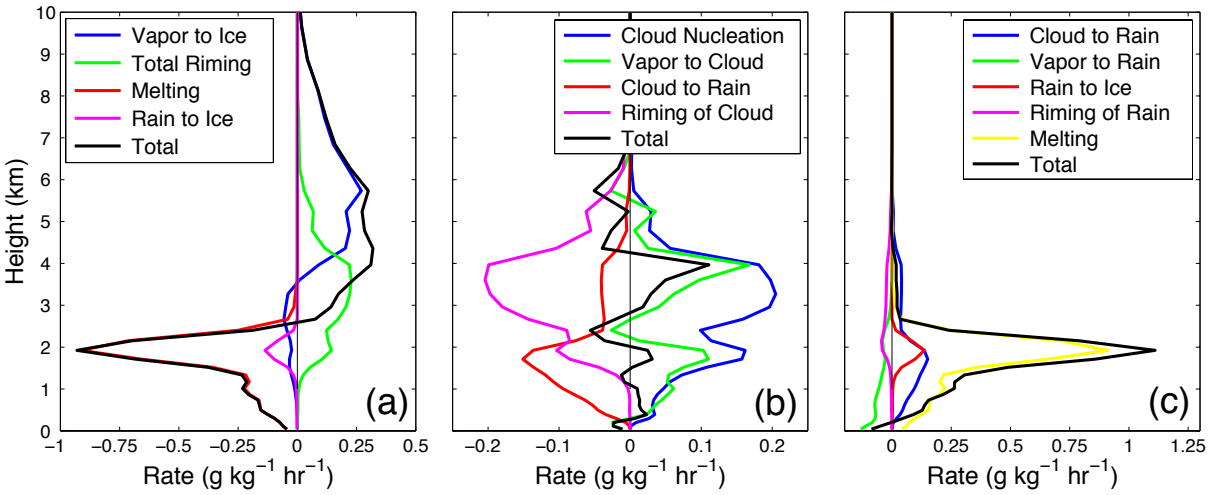

Fig. 2.5. Vertical profiles of each of the major processes contributing to the budget of (a) ice, (b) cloud liquid, and (c) rain. Note the melting level is at 2km.

eventually melt. Sublimation and the collection of ice by rain are minor sinks of ice compared to melting. These results sit between the two cases examined by Rutledge and Hobbs (1983). In the feeder zone of their weak updraft case they found no contribution to the ice budget by riming, whereas in the feeder zone of their mesoscale updraft case they found the riming rate to be 2-3 times greater than the depositional growth rate.

Neither the study by Rutledge and Hobbs (1983) nor that by Gedzelman and Arnold (1993) examined the cloud liquid water budget. The cloud liquid water budget in this study (Fig. 2.5b) shows two peaks in production, one in the mixed phase region of the cloud and one just below the melting level, which is ~2km above ground level. The upper peak is likely caused by updrafts creating supersaturated conditions while the lower peak may exist due to supersaturated conditions being created by the latent cooling due to melting. The cloud nucleation rate is slightly greater than the condensational growth rate at both peaks, and significantly greater in the region between the peaks. The main process contributing to the depletion of cloud liquid at each peak is different. At the upper peak, cloud droplet to rain conversion rates are small and riming rates dominate. However at the lower peak, cloud droplet to rain conversion rates are larger than the riming rate, though riming is still significant at the melting layer. Cloud droplet sizes and rain mixing ratios are both much smaller at the upper peak (Fig. 2.6), which would reduce the rates of auto-conversion and accretion. In total, riming contributes about 33% more to the depletion of cloud liquid than do cloud to rain conversion processes.

Finally the rain budget is shown in Figure 2.5c. Melting of ice is by far the most important producer of rain water, a result found by both Rutledge and Hobbs (1983) and Gedzelman and Arnold (1993). The conversion of cloud liquid water to rain is of secondary importance. These budgets taken as a whole show that ~75% of rain mass is due to melting of

ice, of which half is due to the depositional growth of ice and half due to riming of cloud liquid. The remaining ~25% of rain mass is produced through warm rain processes in this case. The seeder-feeder process is thought to be responsible for the enhancement of precipitation in warm-frontal rainbands (Houze et al., 1981; Rutledge and Hobbs, 1983). Though no distinction has been made between banded and non-banded precipitation in this study, these results also suggest that ice crystals falling through the mixed-phase region of the cloud efficiently collect cloud liquid that would not otherwise be converted to rain; this collection contributes significantly to the total precipitation.

2.5. Sensitivity to Changes in Cloud-Nucleating Aerosol Concentrations

2.5.1. Microphysical cloud properties

The sensitivity of the mass budgets and cloud properties to increases in cloud-nucleating aerosol concentrations will now be discussed by comparing results from the CCN400, CCN800, and CCN1600 simulations. Figure 2.6 shows average vertical profiles of hydrometeor number concentration, diameter, and mixing ratio. Pristine ice, snow, and aggregates (PSA) have been averaged together, graupel and hail (GH) are combined, as are the two cloud droplet modes. Although the responses of each ice species to the sensitivity tests differ, grouping them in this way best shows the overall impact of changes in aerosol concentrations. The PSA number concentration, diameter, and mixing ratio are dominated by aggregates below 8km. Graupel and hail are of the same size, but the hail concentration is about four times larger than that of graupel and dominates the mixing ratio due to its higher density. While hail is not typically associated with warm fronts, the hail stones produced by the model are very small, only about 1 mm, melt quickly, and do not often reach the surface. It is important to note that profiles of mixing ratio

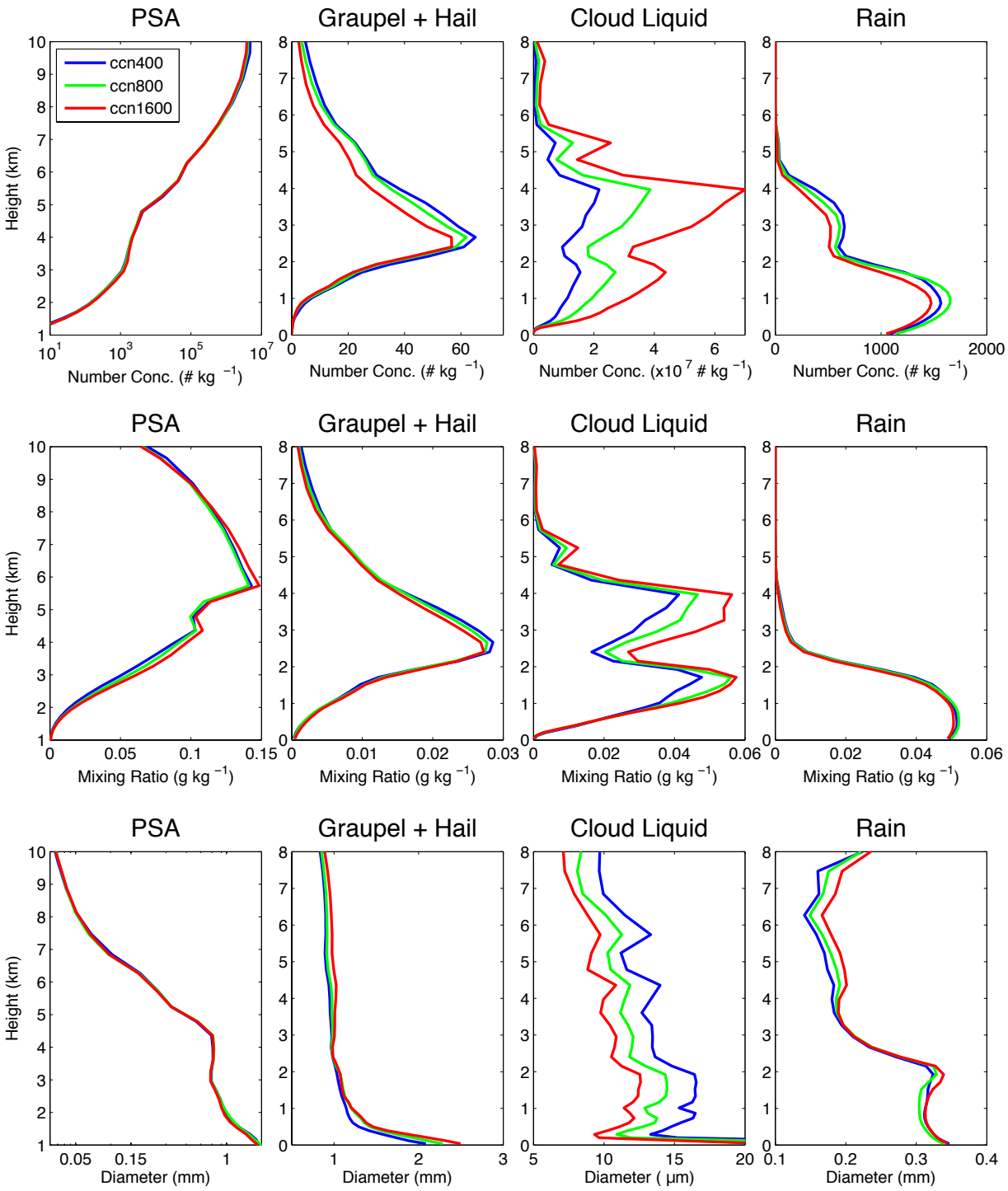

Fig. 2.6. Average vertical profiles of (top row) number concentration, (middle row) mixing ratio, and (bottom row) number concentration for each of the four groups of hydrometeors described in the text. Diameters were averaged only where they were non-zero and weighted by number concentration, but no minimum threshold was used in averaging number concentrations or mixing ratios.

are not expected to match the total budget profiles in Figure 2.5 since advection and sedimentation were not included in the budget calculations.

With increasing pollution cloud droplets are more numerous and smaller which is expected from the cloud albedo effect (Twomey, 1977) and the overall cloud liquid water path is increased. PSA mixing ratio is highest in CCN1600 below 8km, though CCN400 and CCN800 are similar; the trend becomes clearly monotonic at 4km and below. Fewer but larger GH particles exist with enhanced aerosol concentrations; the differences in number decrease below the melting level, but the size discrepancy increases. Overall there is less mass in this category above the melting level in the more polluted cases. Rain shows monotonic trends above 2km where droplets are larger but less numerous and have slightly less total mass with increasing aerosol concentrations. Below 2km, the trends in rain properties are non-monotonic.

Insight into these differences in cloud properties can be gained by examining the changes in budget terms (Fig. 2.7). Cloud condensation rates increase, but not enough to compensate for

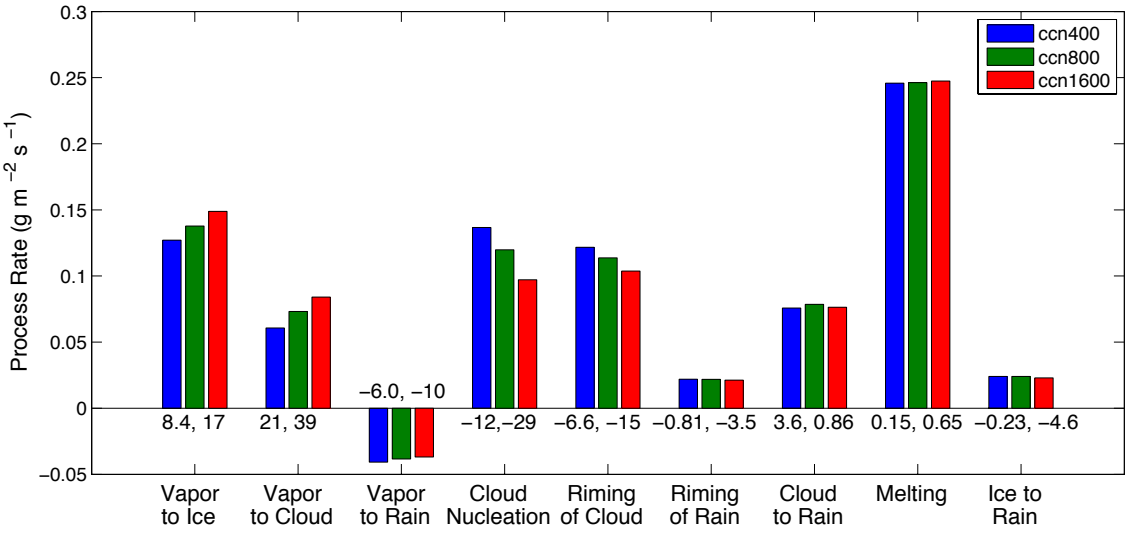

Fig. 2.7. Vertically integrated and averaged rates of each of the major water budget processes. The two numbers printed with each process are the percent change of CCN800 and CCN1600, respectively, from the CCN400 value.

the decrease in cloud nucleation rates such that overall there is less production of cloud liquid with increasing cloud-nucleating aerosol concentrations. The trends in these two terms oppose one another since nucleation and condensation compete for the available water vapor. In the more polluted cases, total condensational growth increases due to the increased total surface area of cloud droplets (not shown), which effectively decreases the supersaturation and inhibits cloud nucleation. The overall increase in cloud liquid mixing ratio seen previously is ultimately a result of decreased riming caused by the decreased size of the cloud droplets.

There are many similarities between warm frontal and orographic clouds – weak to moderate updraft speeds and the presence of a mixed-phase to name two – such that a comparison with results from orographic cloud sensitivity studies is useful. The trends in the three terms discussed above are consistent with the results of Saleeby et al. (2009) who looked at the impacts of cloud condensation nuclei on an orographic snowfall case. In their study though, they found decreased sensitivity to riming rates for CCN concentrations above 500 cm^{-3}, whereas in the present study significant decreases in riming are seen even for the CCN1600 case.

Interestingly, there is very little change in cloud to rain processes across the three simulations such that they do not contribute to changes in mixing ratio of cloud liquid or rain. The same result was seen in one of the simulations of an orographic rain case examined by Muhlbauer et al. (2010). However, this result is in contrast with other purely warm rain studies that show suppressed rain formation in polluted scenarios (e.g. Albrecht, 1989; Xue and Feingold, 2006; Saleeby et al., 2010). It is possible that auto-conversion of cloud droplets to rain is decreasing due to smaller cloud droplet size, but that accretion of cloud droplets by rain is increasing. Since formation of raindrops in this case occurs primarily through melting, they can gain large sizes without growing through auto-conversion of cloud water. This will give the rain

drops a higher terminal velocity than they would otherwise have which would lead to higher collection rates for a given cloud droplet size. It is also possible that the overall greater mass of cloud liquid present may lead to increases in accretion, despite the decrease in cloud droplet size.

In the more polluted simulations PSA mixing ratio increases while that of GH decreases, as discussed above. The budget terms in Figure 2.7 show that vapor deposition increases, while riming decreases with increasing aerosol concentrations. Vapor deposition occurs primarily on the PSA species, so the increase in that process alone explains the increase in PSA mass. Most of the changes in vapor deposition are confined to the mixed phase region of the cloud (not shown). Vapor deposition increases because the Bergeron process is more efficient due to the presence of smaller cloud droplets. That is, under more polluted conditions, smaller cloud droplets are easier to evaporate and new cloud nucleation more easily suppressed in the mixed phase region where supersaturation over ice is higher than that over liquid; ice deposition rates are enhanced as a result. In addition, riming is one pathway for the conversion of PSA to GH; therefore, the decrease in riming further explains the increase of PSA mass as well as the decrease in GH mass with increasing aerosol concentrations above the melting level. At and below the melting level, remaining PSA mass is quickly converted to GH and then to rain. The changes in vapor deposition and riming almost exactly cancel one another, so below the melting level there are no significant differences in the surviving ice mass or in the rain mass produced through melting.

The two largest contributors to rain mass, melting and collision-coalescence, both show little sensitivity to cloud-nucleating aerosol concentration, as discussed above. This explains why there is also little change in rain mixing ratio across the three simulations below the melting

level. As would be expected from this result, there are also only small changes in the average precipitation rates, as seen in Table 2.1.

Table 2.1. Summary statistics of precipitation rate.

Simulation	Precip. Rate (mm/hr)	Percent change from CCN400
CCN400	1.041	-
CCN800	1.056	1.4
CCN1600	1.06	2.1

2.5.2. Local precipitation changes

Although on average the precipitation rates are not very sensitive to aerosol concentration, there are larger changes seen locally. Figure 2.8a shows the time averaged precipitation rates as a function of distance from the front. Precipitation rates are generally the same among cases, although there is a suggestion that the precipitation distribution becomes less broad with increasing aerosol concentrations.

Figure 2.8b again shows time-averaged precipitation rates, but excludes those rates

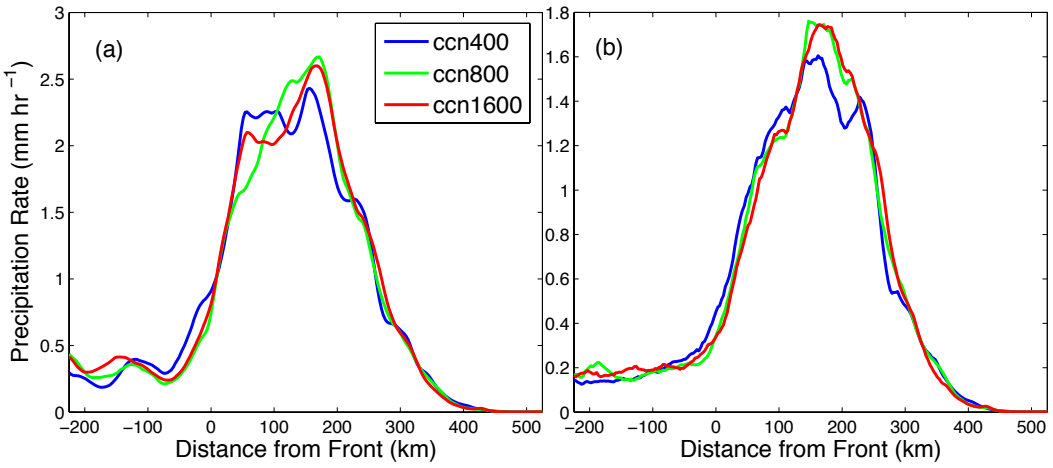

Fig. 2.8. (a) The average precipitation rate as a function of distance from the front. (b) The same as (a) but excluding precipitation rates greater than 5mm hr^{-1}.

greater than 5mm hr^{-1}. The local maxima in CCN400 and CCN1600 in Figure 2.8a around 50km from the front are effectively removed and much clearer trends in precipitation are revealed. There is a delay in the onset of precipitation with increasing cloud-nucleating aerosol concentration such that precipitation is initially shifted about 15-20km downwind. This is similar to the "spillover effect" seen in many orographic snow cases in which precipitation is shifted to the leeward side of a mountain in more polluted conditions (e.g. Givati and Rosenfeld, 2004; Jirak and Cotton, 2006; Lynn et al., 2007; Saleeby et al., 2009). However, further from the front rain rates in the two more polluted simulations have higher intensities at their peaks. Just after these peaks, rain rates are similar across all three cases. Due to the changes in peak rain rates, the difference in average rainfall is still only 2.0% between CCN400 and CCN800 and 1.4% between CCN400 and CCN1600. This is in contrast to the some orographic sensitivity studies which generally find decreases in the overall precipitation due to losses through sublimation of snow and ice crystals on the lee side of the mountain (Lynn et al., 2007). However, in this case, since there is little precipitation where sublimation of ice and evaporation of cloud liquid water is substantial, precipitation cannot be reduced significantly through these processes.

Examination of the vertically integrated processes contributing to rain formation in areas where the rain rate is 5mm hr^{-1} or less (Fig. 2.9) shows that both cloud liquid conversion to rain and melting are suppressed near the front. The suppression from melting is not seen between the CCN800 and CCN1600 cases, but suppression is still clearly evident in the cloud to rain processes. It is not immediately obvious why there is so little difference in melting between CCN800 and CCN1600, especially since riming does not show the same insensitivity. However

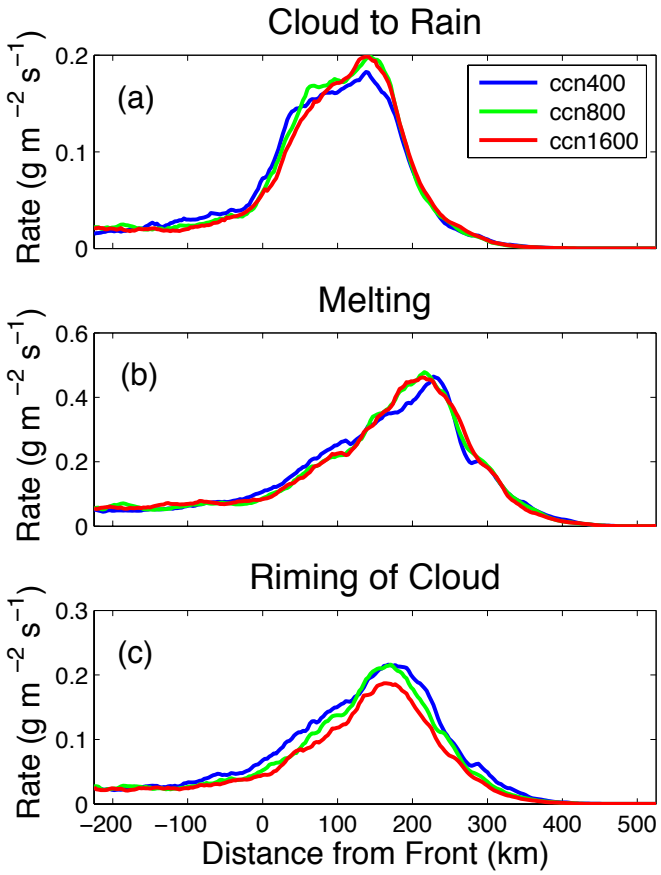

Fig. 2.9. Vertically integrated and averaged values of selected process rates as a function of distance from the front.

the GH particles are larger in CCN1600 and their faster sedimentation rates may be off-setting the decrease in mass due to decreases in riming rates. The increased peak in precipitation in CCN800 and CCN1600 further downwind appears to be due to enhancements in both melting (due to increases in vapor deposition) and cloud to rain processes at these locations.

2.5.3. Latent heating and warm frontal structure

The total latent heating (Fig. 2.10) shows only small differences among the experiments, despite the fact that significant changes were seen in the rates of many cloud processes. There are increases up to 1km, and again between ~3-3.5km. The increase at this latter level is 45% from CCN400 to CCN1600, which is quite significant, although very localized. Decreases are

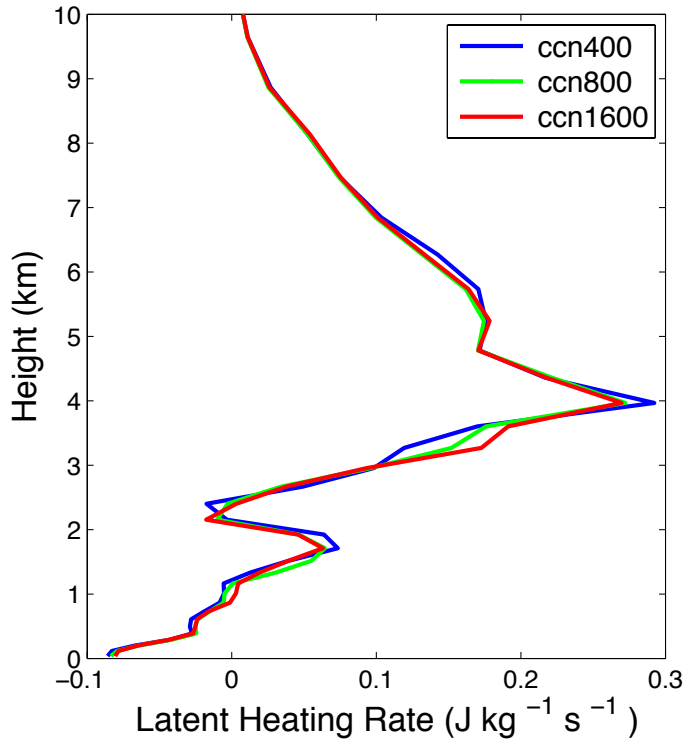

Fig. 2.10. Average vertical profiles of the total latent heating rate.

seen around the melting level as well as ~4km. When vertically integrated, the difference between CCN400 and CCN1600 is only 1.5%. This implies that the changes in warm frontal latent heating from specific cloud processes largely cancel one another when summed.

Finally, vertical profiles of vertical velocities are shown in Figure 2.11. There is on average an increase in vertical velocity throughout the column with increasing aerosol concentrations. Increases in updraft speed (Fig. 2.11b) is only seen in CCN1600 and only between ~4-6km, possibly due to the localized increase in latent heating seen from 3-3.5km. Downdrafts (Fig. 2.11c) show more variability, and on average downdrafts are stronger above 4km. This may be due to enhanced sublimation and evaporation at upper levels (not shown). Regardless, these changes do not seem to have had significant impacts on the warm front as a whole.

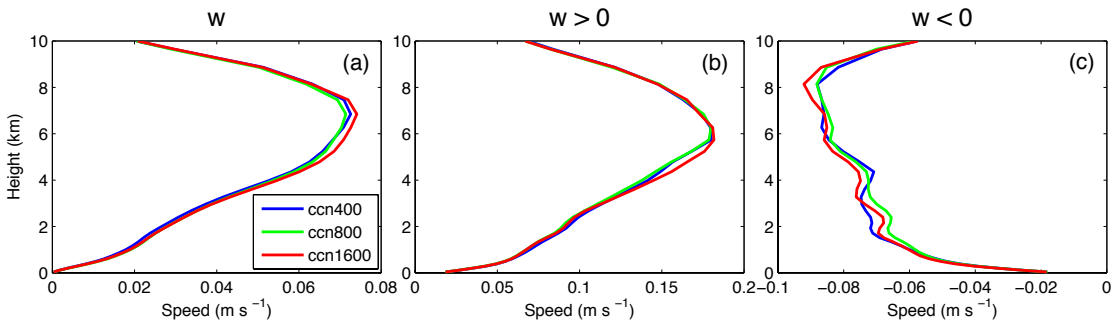

Fig. 2.11. Average vertical profiles of (a) total vertical velocity, (b) updrafts, and (c) downdrafts.

2.6. Conclusions

RAMS was successfully used to simulate a springtime extratropical cyclone that developed and crossed the United States from 9-11 April 2009. First the budgets of cloud ice, cloud liquid water, and rain were examined over the warm front. Deposition and riming both contribute significantly to the total ice mass in this case since updraft speeds were high enough to sustain a deep mixed phase cloud region. Riming is the most significant sink of cloud liquid water, especially in the mixed phase region. Seventy-five percent of the rain is produced through the melting of ice species with the other 25% coming from conversion of cloud droplets to rain. The exact contribution from each varies as a function of distance from the front, as seen in Figure 2.9, with conversion of cloud droplets being fairly constant from 25-175km ahead of the front and melting peaking sharply at 200km ahead of the front. These results of course are specific to the case analyzed here, but do generally agree with the studies of Rutledge and Hobbs (1983) and Gedzelman and Arnold (1993) who both also examined cases in which rain was the predominant hydrometeor at the surface. This suggests that the results are robust for warm fronts in which the seeder-feeder process is dominant. The budgets would of course be expected to differ for colder systems which do not produce rain or ones in which convection is more prominent.

Three sensitivity experiments were conducted in which the profiles of cloud-nucleating aerosol concentrations linearly decreased to 100 cm^{-3} at 4km AGL starting with surface concentrations of 400, 800, and 1600 cm^{-3}. There is a slight shift seen in the distribution of light to moderate precipitation rates where less precipitation falls with increasing aerosol concentration at the surface position of the front, but more falls between 100-200km from the front. In total there is a mere 2% increase in total precipitation from CCN400 to CCN1600.

Significant changes are seen in the budgets of cloud liquid water and ice, but not of rain. A simple schematic is shown in Figure 2.12 that summarizes these results. Due to higher cloud-nucleating aerosol concentrations, cloud droplets are smaller and more numerous. In the mixed-phase region of the cloud, these changes cause enhanced deposition of vapor onto PSA crystals through the Bergeron process, but decrease riming by these particles leading to the creation of fewer GH species. The responses of vapor deposition and riming tend to cancel one another such that similar amounts of total ice are produced, causing little change in rain production from melting, the most important source of rain in warm frontal clouds. This shows then that the mixed-phase part of the cloud has compensating responses that limit the impact of increased

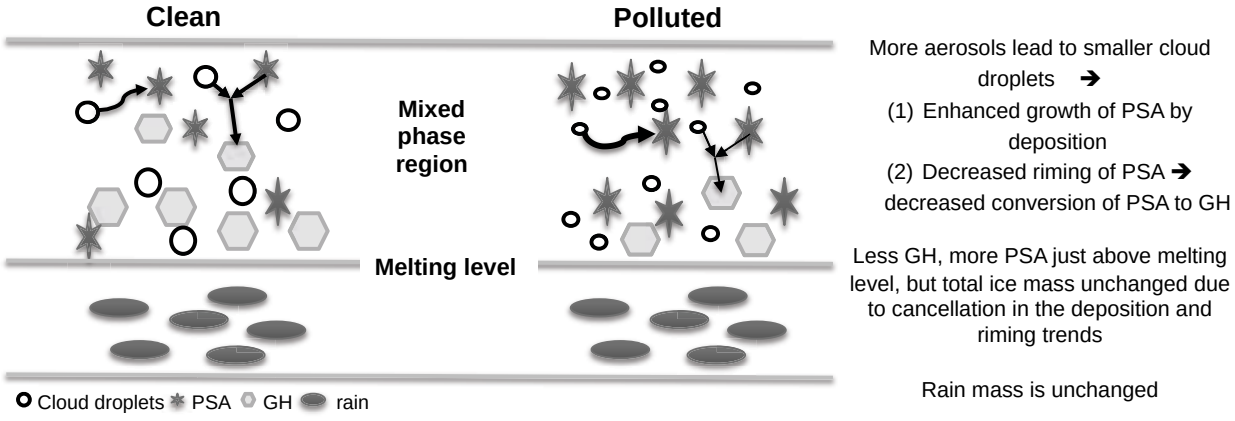

Fig. 2.12. Summary schematic showing the changes to the microphysical properties of the mixed-phase portion of the warm frontal cloud and the total precipitation.

cloud-nucleating aerosols on precipitation. In addition, the compensating responses in cloud processes have prevented large changes in total latent heating. As a result of these, cloud-nucleating aerosols cannot play a strong role in determining the total precipitation or dynamic properties of warm fronts.

Only one case of a spring-season, mostly stratiform warm front was examined in the present study, and it is unclear whether or not these results can be generalized to all warm fronts. The response of more convective fronts or colder systems with less liquid water may be different, as may the response to ice nuclei or giant CCN for storms over the ocean. Investigation into these questions is left for future work. However, an increasing number of sensitivity studies (Stevens and Feingold, 2009; van den Heever et al., 2011; Seifert et al., 2012), including the one here, are finding that the mixed-phase of cloud systems provide built-in buffers that resist wide-scale changes in aerosol concentrations. This trend lends support to the robustness of the conclusions presented here.

III. The role of latent heating in warm frontogenesis

3.1. Introduction

The role of latent heating in frontogenesis, the process through which fronts are formed, has been extensively studied, especially through modeling experiments (Baldwin et al., 1984; Hsie et al., 1984; Thorpe and Emanuel, 1985; Chan and Cho, 1991; Montgomery and Farrell, 1991; Posselt and Martin, 2004). Through these efforts it is known that latent heating strongly influences frontal speed and is important for the mesoscale structure of vertical velocity, rainbands, and the formation of the occlusion in extratropical cyclones. Multiple studies have shown that vertical velocities are increased, updrafts are narrowed, and the horizontal ageostrophic circulation is increased when the effects of latent heating are included in numerical models (Baldwin et al., 1984; Thorpe and Emanuel, 1985; Han et al., 2007). The contributions of latent heating to frontogenesis at midlevels seems to be particularly important for the formation of rain bands (Novak et al., 2009; Baxter et al., 2011). However the mechanisms through which all of these impacts are realized are not well understood. For example, it is unclear if frontal speed is increased due to increases in the cross-frontal circulation in the presence of latent heating or whether it is increased due to the creation and propagation of potential vorticity (PV) anomalies that act to alter the wind fields (Reeves and Lackmann, 2005).

Furthermore, aside from condensation, which is the focus of most of the studies reported in the literature, there has been little examination of the relative importance of individual microphysical processes in latent heating and frontogenesis. Evaporation and sublimation have been found to enhance downdrafts (Huang and Emanuel, 1991; Parker and Thorpe, 1995; Clough et al., 2000) and melting may accelerate surface frontogenesis in winter storms (Szeto and Stewart, 1997). All but one of these studies employed an idealized 1- or 2-dimensional model

framework and all use relatively simple microphysics parameterizations. A better understanding of the role of individual processes could help to explain the spectrum of responses to latent heating that have been observed in fronts.

This study will focus on the direct role of latent heating, both total latent heating and latent heating from individual cloud processes, on the warm front. Joos and Wernli (2011) examined the role of vapor deposition, cloud condensation, riming, and melting in the modification of potential vorticity along the warm conveyor belt and in doing so presented a budget of latent heating along the warm conveyor belt. This study will extend that work by developing a budget for latent heating over the warm front that includes cloud condensation and riming in addition to those processes presented by Joos and Wernli (2011), and by assessing the role of each latent heat process to horizontal and vertical frontogenesis equations. Furthermore, the horizontal and vertical components of frontogenesis will be combined in a novel way to examine the rate of change of the frontal slope in order to evaluate the overall impact of latent heating on the thermal structure of the front.

3.2. Methods

3.2.1. Model setup and storm evolution

This study examines the warm front of an extratropical cyclone that crossed the United States from 9-11 April 2009. The Regional Atmospheric Modeling System (RAMS) (Pielke, et al., 1992; Cotton et al., 2003) was used to simulate the storm. The setup consisted of two nested grids, with the outer grid covering the majority of the United States at 15km horizontal grid spacing and the inner grid extending from the Rockies to the coast of Maine at 3km horizontal grid spacing. The location of the inner grid is depicted in Figure 3.1. Both grids contained 45 vertical levels with 75m spacing at the surface expanding to 1km spacing near the model top. A

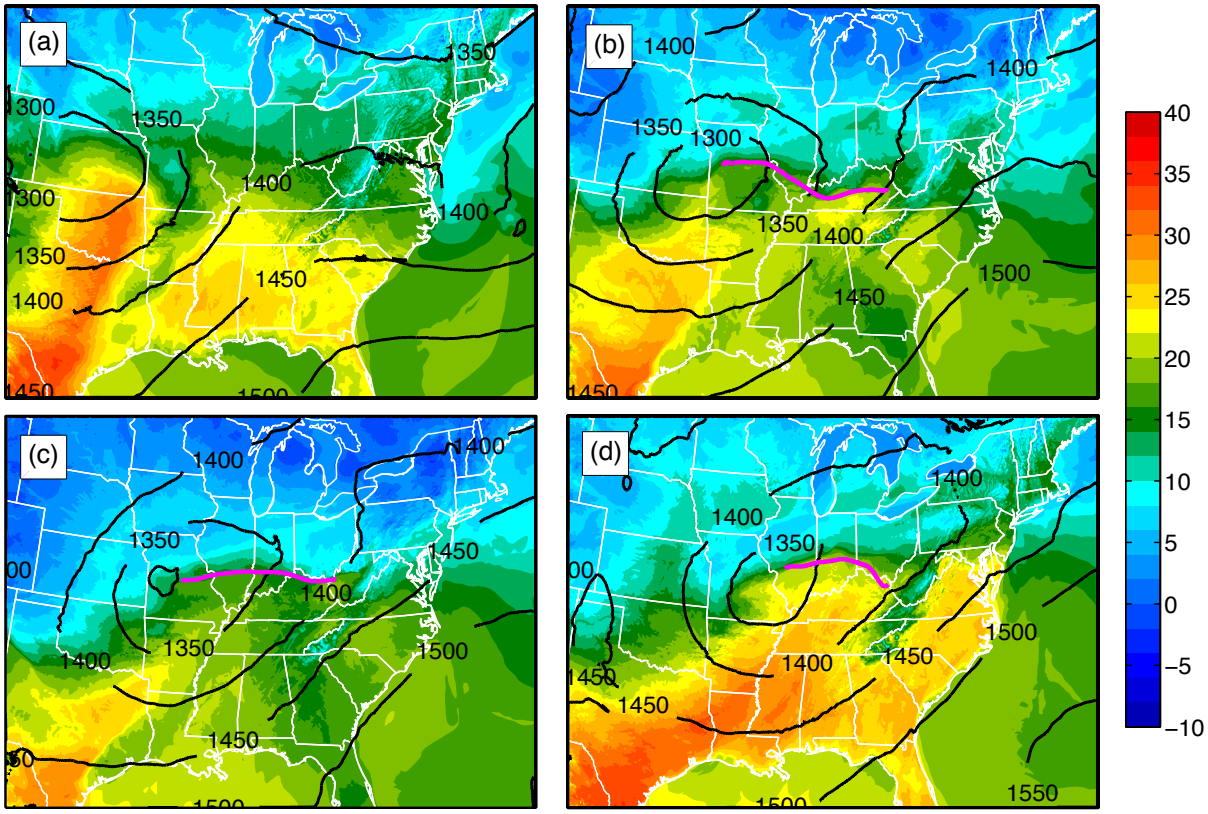

Fig. 3.1. RAMS output from the inner grid of surface temperature (°C, shaded), 850mb geopotential height (contoured), and the objectively analyzed warm front location (heavy pink) at simulation hours (a) 18, (b) 30, (c) 36, and (d) 42.

two-moment bin-emulating bulk microphysical scheme (Saleeby and Cotton, 2004, 2007) that prognoses the mixing ratio and number concentration of five ice species (pristine ice, snow, aggregates, graupel, and hail) and three liquid species (two cloud droplet modes and rain) and that also tracks the rates of many microphysical processes was used.

The model was initialized at 00 UTC 9 April 2009 using the corresponding Global Forecast System (GFS) analysis file and integrated for 48 hours with subsequent GFS analysis files being used to nudge the lateral boundaries. Figure 3.1 shows surface analyses of various storm characteristics over the course of the simulation. It possessed an elongated, well-defined warm front that persisted for about 16 hours and caused widespread precipitation from Missouri

to Ohio. A secondary boundary, located south of the storm center, was associated with a severe weather outbreak in the southeast United States. The model reproduced the observed warm frontal structure and accumulated precipitation well (Igel et al. (2012)).

3.2.2. Objective front detection

An objective front detection algorithm based on the method of Hewson (1998) was applied to the output to locate the warm front. Briefly, fronts are identified where $\left|\nabla\left|\nabla\theta\right|\right|$ at the surface is zero, and then the geostrophic wind is used to separate warm from cold fronts. Here the gradient operator acts only in the horizontal directions. Additional masks were applied to remove fronts that were detected due to land-water boundaries, the southern boundary associated with the severe weather outbreak, and fronts that were not continuous in time. The algorithm was run for every output hour. Three of the objectively identified fronts are shown in Figure 3.1 where it can be seen that the fronts lie in the zonal direction. The model output from the inner grid was subsetted relative to the front. Raw fields were smoothed by replacing each data point with the average of the points in a 7x7 box centered on itself; then the derived fields were calculated. All fields were averaged over hours 27-42 of the simulation in which the warm front was well-defined, and in the along-front direction to obtain zonally-averaged cross sections perpendicular to the front.

Figure 3.2 shows the average cross-sections of potential temperature and meridional and vertical winds. As expected, the surface position of the front is located on the warm side of the baroclinic zone and air is rising up and over the front. There is convergence present across the frontal zone in the meridional wind field and the maximum winds are found 0.5-1 km above the surface. Figure 3.3 shows average cross sections of the horizontal and vertical gradients of potential temperature. These figures further confirm that the frontal detection algorithm has been

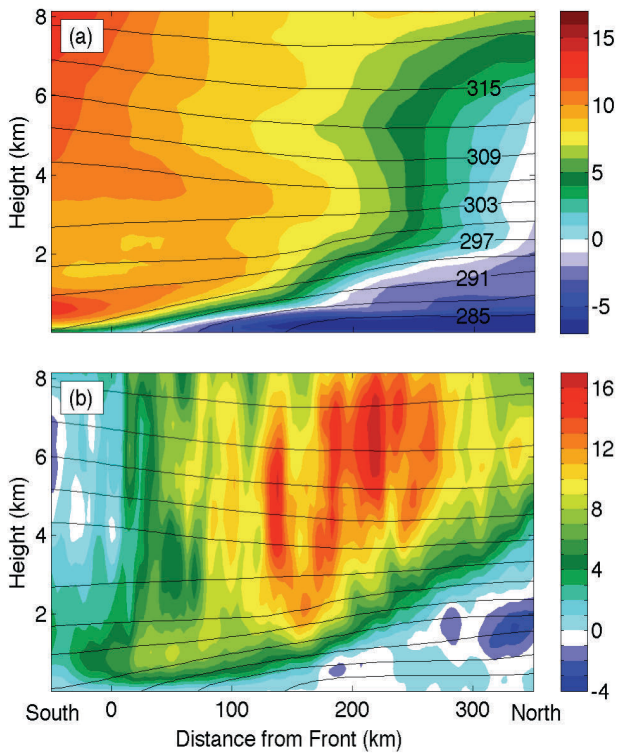

Fig. 3.2. Composite cross sections of (a) cross-front wind velocity (m s^{-1}) and (b) vertical velocity (cm s^{-1}). The thin black lines are isentropes (K).

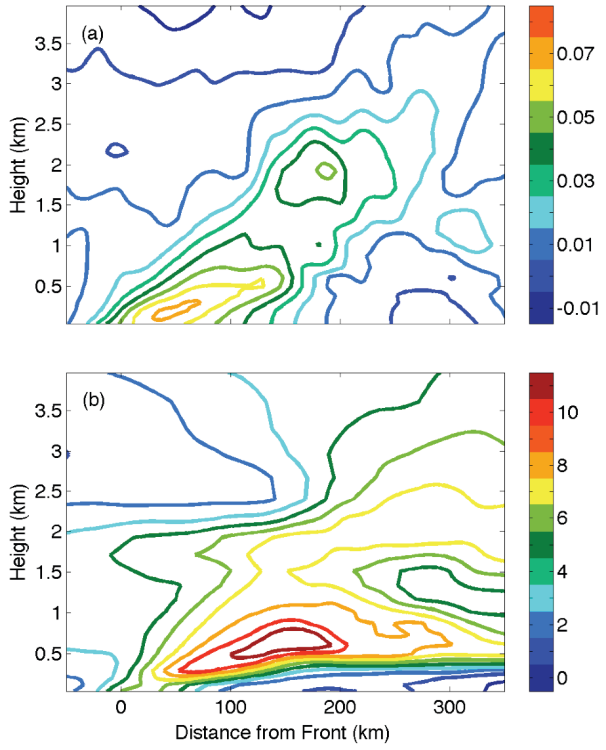

Fig. 3.3. (a) Negative of the horizontal gradient and (b) vertical gradient of potential temperature in K km^{-1}. Note that the vertical axis is different from that in Fig. 2.

successful. Furthermore, the ridge of maximum values extending from the surface in these fields indicate the position of the frontal surface and will aid discussion below.

The reader is referred to Igel et al. (2012) for further details on the evolution of the simulated storm and the objective frontal detection algorithm, should they be interested.

3.2.3. Frontogenesis equations

Both the horizontal and vertical components of frontogenesis will be examined. The horizontal cross-front component is expressed as

$$\frac{d}{dt}\left(-\frac{d\theta}{dy}\right) = \overbrace{\frac{\partial u}{\partial y}\frac{\partial \theta}{\partial x}}^{a} + \overbrace{\frac{\partial v}{\partial y}\frac{\partial \theta}{\partial y}}^{b} + \overbrace{\frac{\partial w}{\partial y}\frac{\partial \theta}{\partial z}}^{c} \overbrace{- \frac{\theta}{T c_p}\frac{\partial}{\partial y}\left(\frac{dQ}{dt}\right)}^{d} \qquad (3.1)$$

and is similar to the form used by Keyser and Pecnick (1985). The coordinate axes are defined such that the *x*-axis is in the zonal direction and nearly parallel to the front (see Fig. 3.1), the *y*-axis points to the north, and *z* is defined as the height above the surface. In the above equation *u* is the zonal wind velocity, *v* is the meridional wind velocity, *w* is the vertical velocity, *T* is the temperature, c_p is the specific heat of air at constant pressure, and *dQ/dt* is the diabatic heating rate. There are four terms on the right-hand side (RHS) of Eq. 3.1: shearing deformation (*a*), confluent deformation (*b*), tilting (*c*), and diabatic contributions (*d*). Previous work has found that shearing deformation is much smaller than confluent deformation in the region of warm fronts due to small zonal gradients in potential temperature (Han et al., 2007). The same result is seen found in this analysis (not shown) and hence any term containing the zonal gradient of potential temperature here and in the equations to follow will be neglected in the analysis. In addition, no equation for the evolution of $d\theta/dx$ is needed since it is assumed to be small. The last term, the diabatic contribution, takes into account processes such as latent heating, radiation, and friction; however, this study will only consider the contributions of latent heating processes to the diabatic term.

Frontal surfaces are known to be areas of high static stability, yet few studies have examined the evolution of the frontal structure in the vertical direction or the effect of environmental static stability on fronts. Rather most of the attention has been given to the evolution of horizontal potential temperature gradients, the quantity most often used to identify fronts. However, Bannon (1984) found that fronts evolving in environments with relatively high static stability move more slowly, possess weaker horizontal potential temperature gradients, and are less steeply sloped than fronts evolving in environments with lower static stability due to suppressed vertical motions. This suggests that the vertical structure of frontal zones can be

important for the evolution of the front as a whole and should not be so routinely disregarded in frontal studies.

The vertical component of the frontogenesis equation can be used to understand the formation of zones of high static stability and inversions that are associated with fronts (Miller, 1948). Similarly to the equation for the horizontal component (Eq. 3.1), it can be expressed as

$$\frac{d}{dt}\left(\frac{d\theta}{dz}\right) = -\frac{\partial u}{\partial z}\frac{\partial \theta}{\partial x} \overbrace{-\frac{\partial v}{\partial z}\frac{\partial \theta}{\partial y} - \frac{\partial w}{\partial z}\frac{\partial \theta}{\partial z}}^{e} + \overbrace{\frac{\theta}{T c_p}\frac{\partial}{\partial z}\left(\frac{dQ}{dt}\right)}^{f}. \qquad (3.2)$$

Again, the first term on the RHS will be neglected. Term *e* in Eq. 3.2 will be called the "dynamic term" and term *f* the "diabatic term." Considering only the dynamic terms of Eqs. 3.1 and 3.2, one can see that the only difference is that the partial derivatives involving wind speeds are taken with respect to different coordinates. A typical value for $\partial v/\partial z$ is ~10 m s^{-1} (100 km)$^{-1}$ whereas $\partial v/\partial y$ is about 100x greater at ~10 m s^{-1} km^{-1}. A similar relationship exists between the meridional and vertical derivatives of *w*. Therefore vertical frontogenesis should be at least ~2 orders of magnitude greater than horizontal frontogenesis.

Positive vertical frontogenesis is needed to form the stable layer associated with fronts, but if vertical frontogenesis is strong enough, then it will act to flatten the isentropes in a frontal zone, or in other words, decrease their slope. A decreased slope should lead to decreases in vertical velocities and in that sense it weakens the front, even if horizontal frontogenesis is positive, as shown in the schematic in Figure 3.4. To get at the balance between the vertical and horizontal components of frontogenesis, a new equation is introduced that expresses the rate of change of the slope of the isentropes. First, the chain rule can be used to express the slope of the isentropes as the negative ratio of the horizontal θ gradient to the vertical θ gradient as follows:

$$d\theta(y,z) = \frac{d\theta}{dy}dy + \frac{d\theta}{dz}dz = 0 \qquad (3.3)$$

$$\left.\frac{dz}{dy}\right|_{\theta} = \frac{-\frac{d\theta}{dy}}{\frac{d\theta}{dz}}. \tag{3.4}$$

Next the total time derivative is taken on both sides of Eq. 3.4. One can invoke the chain rule again to express the time rate of change of the slope as

$$\frac{d}{dt}\left(\left.\frac{dz}{dy}\right|_{\theta}\right) = \frac{\frac{d\theta}{dz}\frac{d}{dt}\left(-\frac{d\theta}{dy}\right) + \frac{d\theta}{dy}\frac{d}{dt}\left(\frac{d\theta}{dz}\right)}{\left(\frac{d\theta}{dz}\right)^2}. \tag{3.5}$$

The left-hand side of Eq. 3.5 is defined as the slope tendency of the front. It is a function of the meridional and vertical θ gradients, and the horizontal and vertical frontogenesis rates. A similar equation could be constructed for the slope in the zonal direction as well. As shown previously, horizontal frontogenesis is ~100x smaller than vertical frontogenesis; however $d\theta/dz$ is ~100x greater than $d\theta/dy$ along the frontal surface (Fig. 3.3). Therefore, the terms in the numerator of Eq. 3.5 should be of equal magnitude and compete for dominance.

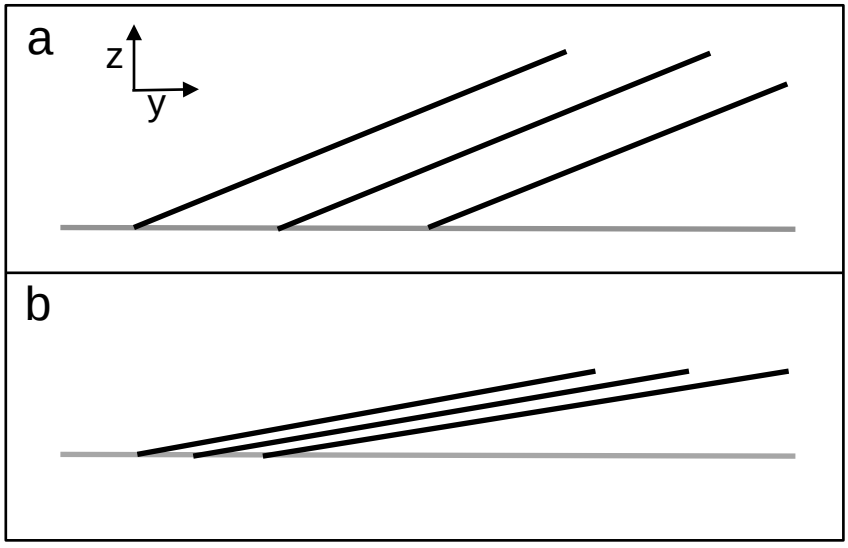

Fig. 3.4. A simple schematic of a warm front where the black lines represent isentropes. In (b), both the horizontal and vertical gradient of potential temperature have increased over their values in (a), but the slope has decreased and so in that sense the front has weakened. See the text for further discussion.

The expressions for the two components of frontogenesis (Eqs. 3.1 and 3.2) can be substituted into Eq. 3.5. After reordering the terms, the slope tendency can be written as

$$\frac{d}{dt}\left(\left.\frac{dz}{dy}\right|_{\theta}\right) = \frac{\overbrace{\frac{d\theta}{dz}\left[\frac{\partial v}{\partial y}\frac{\partial \theta}{\partial y}+\frac{\partial w}{\partial y}\frac{\partial \theta}{\partial z}\right]+\frac{d\theta}{dy}\left[-\frac{\partial v}{\partial z}\frac{\partial \theta}{\partial y}-\frac{\partial w}{\partial z}\frac{\partial \theta}{\partial z}\right]}^{g}\overbrace{-\frac{\theta}{Tc_p}\left[\frac{d\theta}{dz}\frac{\partial}{\partial y}\left(\frac{dQ}{dt}\right)+\frac{d\theta}{dy}\frac{\partial}{\partial z}\left(\frac{dQ}{dt}\right)\right]}^{h}}{\left(\frac{d\theta}{dz}\right)^2}. \quad (3.6)$$

The terms with zonal gradients of potential temperature have been dropped since it was assumed previously that they are negligible. Term *g* in Eq. 3.6 is the dynamic contribution to the slope tendency and term *h* the diabatic contribution. The units of the slope tendency will be expressed as m km^{-1} hr^{-1} and can be interpreted as the rise (or fall) in meters of an isentrope per kilometer in the horizontal per hour. A typical slope of the warm front in this simulation is ~10 m km^{-1}. This is in agreement with the observations of Kemppi and Sinclair (2011) who found warm frontal slopes ranging from 6-18 m km^{-1}.

3.3. Results

3.3.1. Latent heating budget

Figure 3.5 shows the zonally-averaged spatial distribution of the six primary microphysical processes that contribute to latent heating within the warm frontal cloud, namely vapor deposition/sublimation onto/of all ice species (vapor to ice), condensation/evaporation of cloud droplets (vapor to cloud) and rain (vapor to rain), cloud droplet nucleation (cloud nucleation), riming of cloud droplets and rain by ice species (riming), and conversion of ice species to liquid species (melting). Clearly vapor deposition (Fig. 3.5a) onto ice is the most

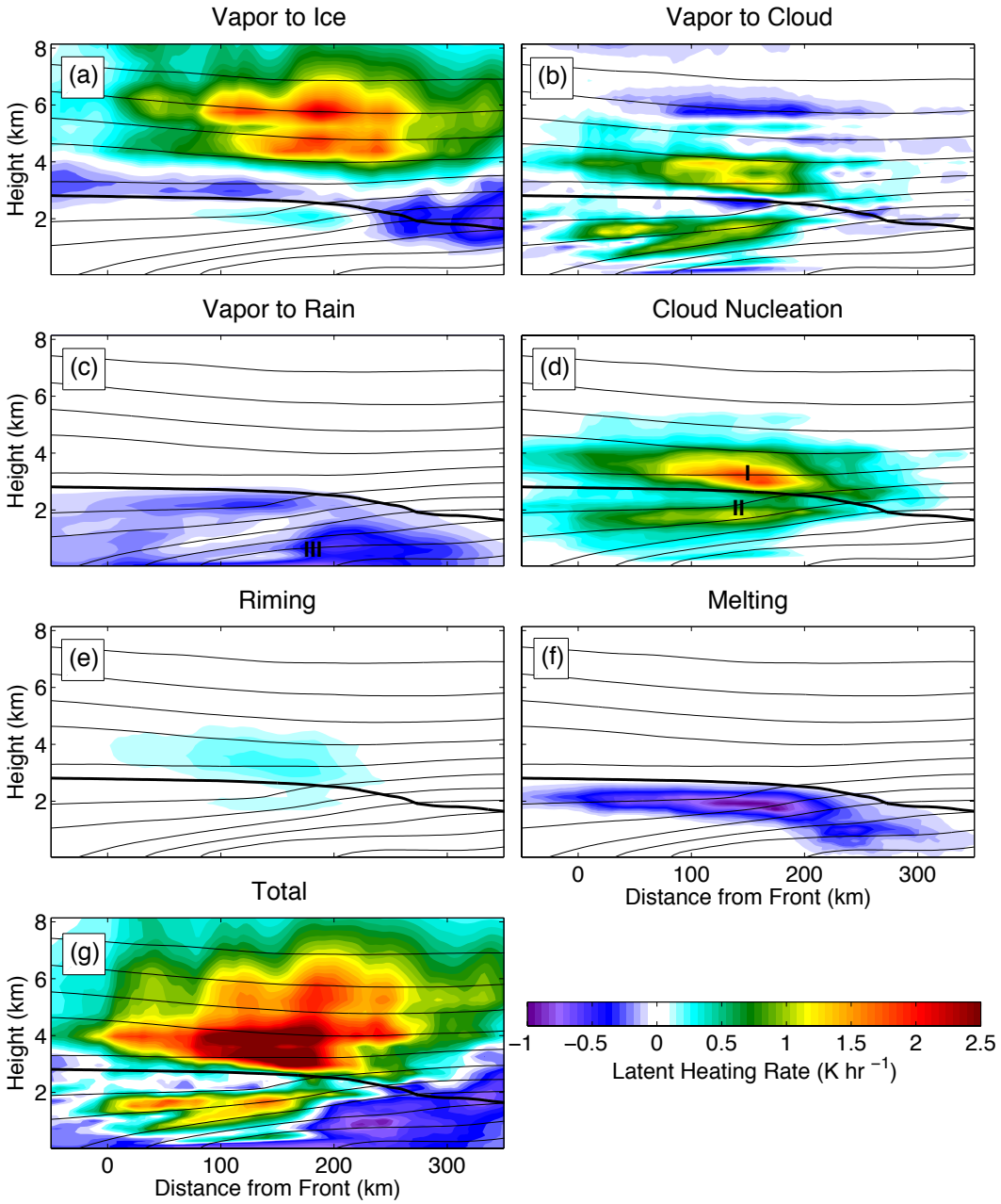

Fig. 3.5. Composite cross sections of the latent heating rate (K hr^{-1}) of (a-f) the six most important microphysical processes acting along the warm front and (g) their total. The thin black lines are isentropes and the thick black line is the 0° isotherm.

dominant, both in the absolute maximum at any point and in total when integrated over the domain. However since latent heat release associated with this process is mostly confined to 4km and above, it has little direct influence on the frontal zone itself. That is not to say that it

cannot contribute to the creation or destruction of upper level potential vorticity, which can of course influence lower levels and the front, but only to say that the heating does not have a direct impact on the isentropic structure of the warm frontal surface.

Latent heating from vapor condensation (Fig. 3.5b) and cloud nucleation (Fig. 3.5d) rival that of vapor deposition in magnitude, but are much closer spatially to the frontal surface and can therefore have a larger influence. Two maxima exist in the cloud condensation and cloud nucleation fields, labeled I and II in Figure 3.5d. The upper peak is due to supersaturated conditions associated with peaks in updraft velocities while the lower peak is associated with the melting layer (Fig. 3.5f), where the latent cooling by melting is helping to create supersaturated conditions (Woods et al., 2008). Though the heat absorbed per kilogram of melting ice is an order of magnitude less than that associated with evaporation or sublimation, the maximum latent cooling from melting has a similar magnitude to the maxima of vapor to ice, vapor to cloud, and cloud nucleation. This is because the ice must melt in a very shallow layer (Clough et al., 2000) and therefore the rate of melting is about an order of magnitude greater than that of any other microphysical process. However since the melting is collocated with condensation and nucleation, there is little net latent heating or cooling directly beneath the melting level (Fig. 3.5g).

Evaporation of rain (Fig. 3.5c) is widespread beneath the melting level and maximizes around 200km ahead of the front at location III due to low relative humidity in the dry continental air mass and because the rain is heaviest there due to a maximum in the vertically integrated melting rate. Overall, the relative contributions of condensation, deposition, and evaporation of rain are in agreement with the findings of Joos and Wernli (2011) who examined the latent heating budget of parcel trajectories along the warm conveyor belt. In their study

latent cooling due to melting was much less, but this would be expected for parcels with predominantly rising trajectories upwind of the front that do not pass through the area of strongest melting.

Finally, riming contributes very little to the total latent heating. Like melting rates, riming rates would need to be an order of magnitude larger than those of liquid-vapor or ice-vapor processes in order to achieve high latent heating rates. However since riming is not confined to occur in a shallow layer like melting is, these high rates are not achieved.

3.3.2. Horizontal frontogenesis terms

We will now examine the rates of horizontal frontogenesis associated with each of the microphysical processes (Eq. 3.1, term *d*; Fig. 3.6) and how they compare to the rates from the dynamic terms (Eqs. 3.1, terms *b*, *c*; Fig. 3.7). Horizontal frontogenesis due to cloud condensation (Fig. 3.6b) is largest, particularly along the frontal surface from 25-200km ahead of the front (location I in Fig. 3.6b). Cloud nucleation (Fig. 3.6d) also produces some significant values, but not until ~150-200km ahead of the front at location I where they serve to reinforce the pattern found in cloud condensation. Melting shows some high frontolysis rates at location II (Fig. 3.6f), but they are largely negated by the frontogenesis due to the cloud liquid processes (Fig. 3.6b, c). Evaporation of rain (Fig. 3.6c) plays a modest role and also serves to strengthen the frontogenesis associated with cloud condensation at location III. Vapor deposition (Fig. 3.6a) does contribute somewhat to frontogenesis at midlevels far ahead of the front (location IV) and further counteracts the frontolysis due to melting. As expected from the previous section, riming is negligible.

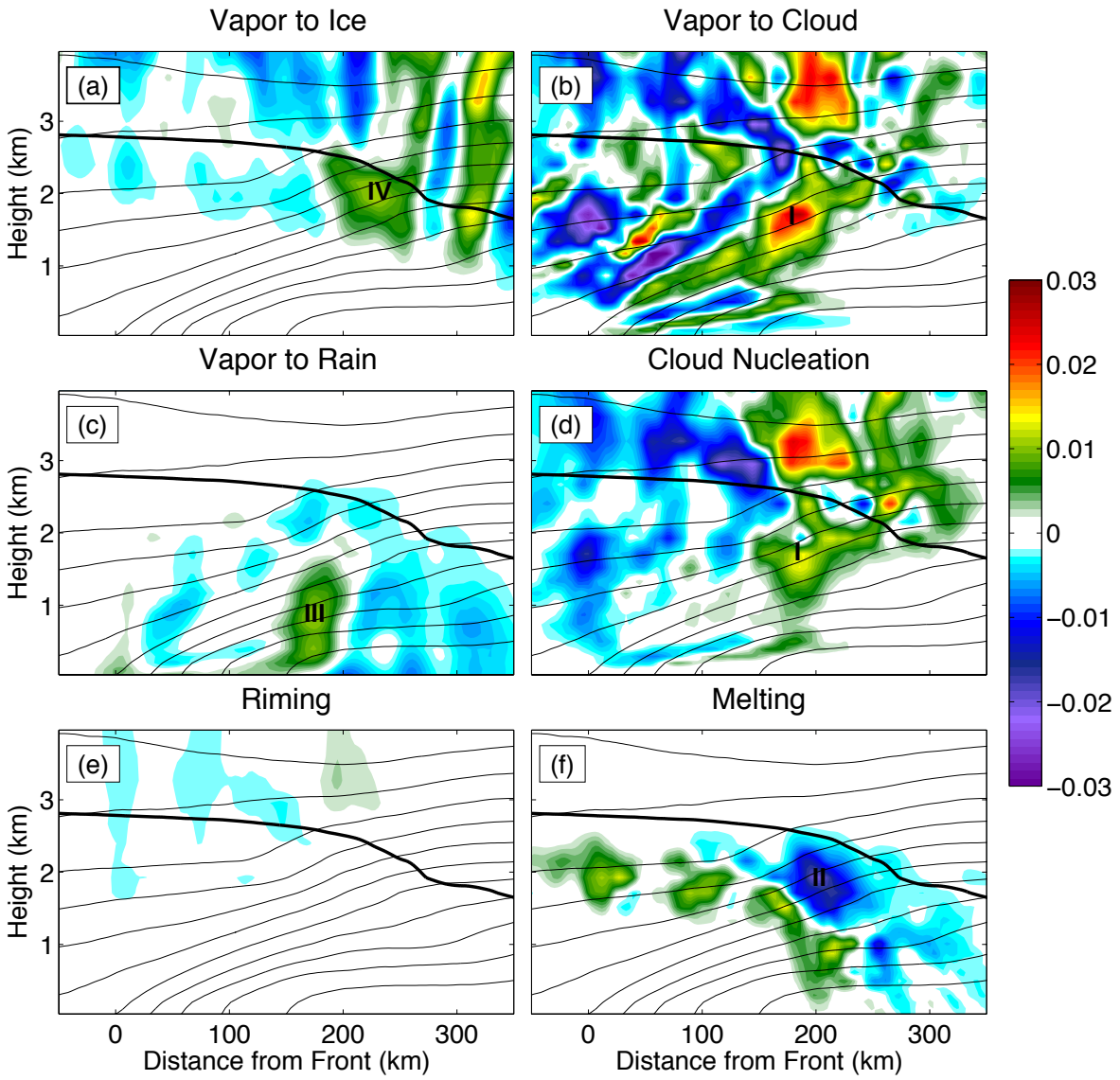

Fig. 3.6. Same as Fig. 5 except horizontal frontogenesis (K km^{-1} hr $^{-1}$). Note that the upper limit on the vertical axis is reduced from that used in Figure 5.

The deformation, tilting, and total diabatic terms are shown in Figure 3.7. The deformation term (Fig. 3.7a) is the most spatially uniform of the three and contributes most to frontal building at and just above the surface. The tilting term (Fig. 3.7b) is mostly frontolytic which agrees with the results of previous studies (Han et al. (2007) and references therein) that showed that the tilting and deformation terms should generally oppose one another in sign. Han

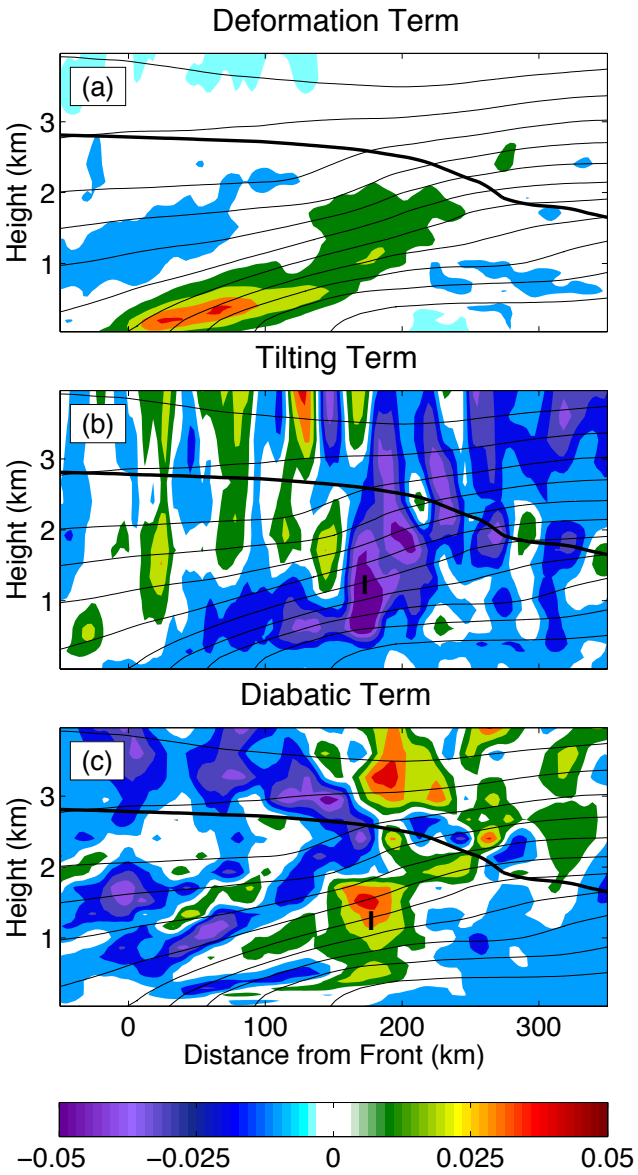

Fig. 3.7. Composite cross sections of the a) deformation, b) tilting, and c) diabatic terms of the horizontal frontogenesis equation (K km^{-1} hr $^{-1}$).

et al. (2007) also showed that the tilting and diabatic terms should oppose one another, a result which is seen here for the maximum in each term located 150-200km ahead of the front at location I in Fig. 3.7. In the horizontal then, the primary role of the diabatic term is to increase frontogenesis between ~0.5-2km above the surface, but ~175km from the surface location of the front. This is consistent with Hsie, et al. (1984) who found the largest increases in the horizontal

temperature gradient at midlevels when condensation and evaporation were included in an idealized simulation of a cold front.

3.3.3. Vertical terms

When considering microphysical processes, one would expect large gradients both in the vertical direction as well in the horizontal direction. Indeed this is the case, as seen in Figure 3.8.

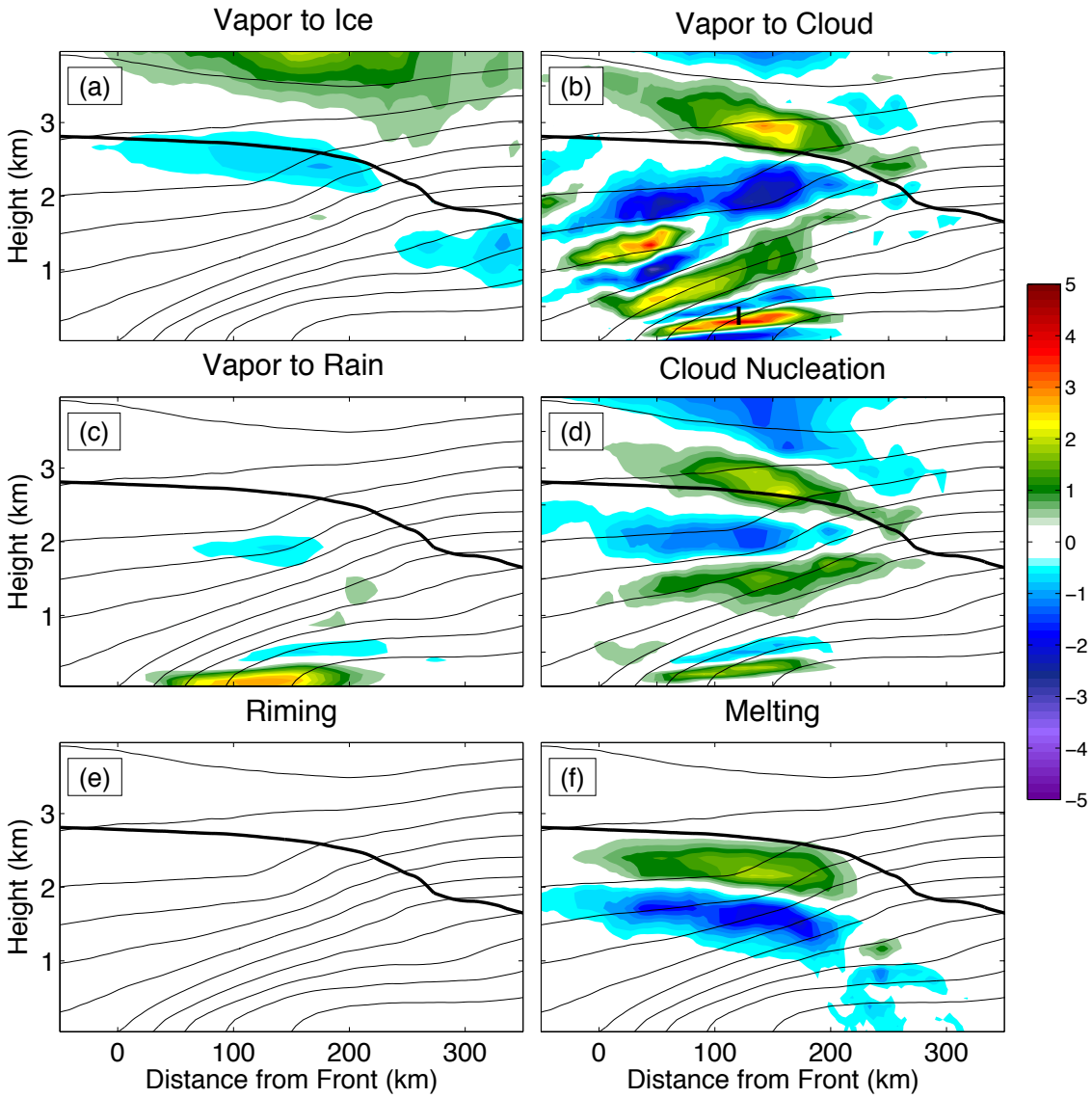

Fig. 3.8. Same as Fig. 6 except vertical frontogenesis (K km^{-1} hr $^{-1}$).

Distinct layers of frontogenesis and frontolysis exist in all fields except riming. Vapor deposition (Fig. 3.8a) is still too far removed from the frontal surface to play much of a role and the effects of melting (Fig. 3.8f) and cloud liquid processes (Fig. 3.8b, d) again oppose each other to some extent just below the freezing level. Some of the highest rates of frontogenesis occur just above the surface in association with the cloud boundary (location I in Fig. 3.8b) where there is a sharp transition from condensation to evaporation (Fig. 3.5b). Just below this,

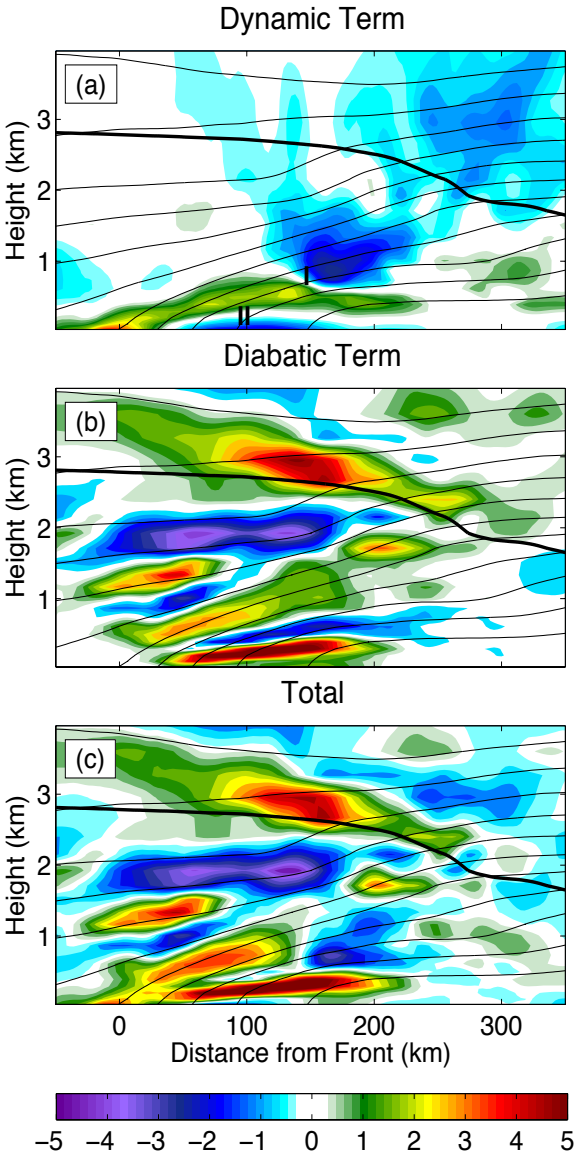

Fig. 3.9. Composite cross sections of the a) dynamic and b) diabatic terms of the vertical frontogenesis equation and c) their total (K km^{-1} hr $^{-1}$).

evaporation of rain (Fig. 8c) also has a very strong signal that is confined to a shallow layer near the surface. Furthermore, the sum of these terms, the total diabatic term (Fig. 3.9b), is almost everywhere larger than the dynamic term (Fig. 3.9a) and dominates the total vertical frontogenesis (Fig. 3.9c).

The vertical dynamic term is positive along the frontal surface out to ~150km at which point it becomes frontolytic (location I, Fig. 3.9a) because vertical gradients in *w* (Fig. 3.2b) begin to dominate the dynamic term. At the surface, ahead of the front at location II, the dynamic term is also frontolytic. This latter shift occurs because the strongest meridional winds occur just above the surface (Fig. 3.2a) leading to a reversal in wind shear that changes the sign of the first term in *e* in Eq. 3.2.

3.3.4. Slope change

Finally Figure 3.10 shows the dynamic, diabatic, and total slope tendencies of the front. Even though the potential temperature field is smoothed, static stability is near zero at some grid points such that the calculation of slope tendency yields unrealistically large numbers due to division by the square of static stability in Eq. 3.5. Therefore all rates greater than 100 m km^{-1} hr^{-1} have been removed. This is a subjective threshold, but the pattern of slope tendency was seen to be insensitive to the choice of threshold value.

There is strong dynamic positive slope tendency right at the surface (location I, Fig. 3.10a) associated with the elevation of the strongest low-level winds (Fig. 3.2a). Elsewhere along the frontal surface positive and negative values can be found; this pattern reflects the competing nature of the confluent and tilting terms of the horizontal frontogenesis. There is significant suppression of the isentropes below the melting level at and beyond 175 km from the surface front that is primarily caused by frontolytic tilting in the horizontal (compare to Fig.

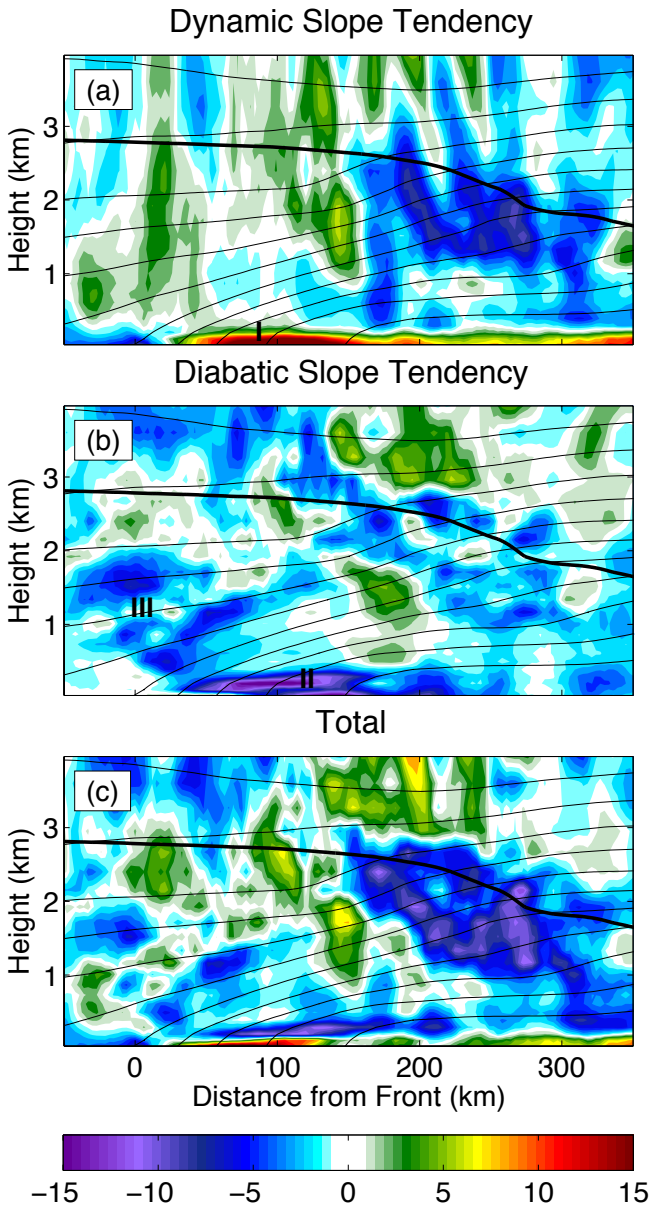

Fig. 3.10. The same as Fig. 9 except for slope tendency (m km^{-1} hr $^{-1}$).

3.7b). In this region the dynamic slope tendency dominates the total slope tendency seen in Figure 3.10c.

The diabatic slope tendency is generally small around the melting level and along the frontal surface despite large values of frontogenesis/frontolysis there, especially in the vertical. This is because the horizontal and vertical diabatic frontogenesis terms often have the same sign

in these regions, leading to cancellation of the two terms in *h* in Eq. 3.6 (the horizontal and vertical gradients of potential temperature have opposite signs nearly everywhere). At and just above the surface however, there is strong suppression of the isentropes associated with the evaporation of cloud and rain (location II, Fig. 3.10b) that counteracts the dynamic slope tendency. Upwind of the front (location III) the diabatic term is also negative and suppresses much of the change in slope being produced there through dynamic processes (Fig. 3.10c). In fact, the diabatic slope tendency is almost everywhere negative, indicating that latent heating consistently acts to decrease the slope of the front and weaken the updrafts forced by dynamics. That is not to say that latent heating does not locally enhance updrafts, which it does, but that latent heating causes the frontal structure itself to become less favorable for the formation of updrafts through dry processes.

3.4. Conclusions

RAMS has been used to simulate an extratropical cyclone at high resolution. First the latent heating budget associated with the warm front was examined. We found that vapor deposition is the largest source of latent heat, but that condensation and the nucleation of cloud droplets contributed most significantly near the frontal surface. Melting provided the largest source of latent cooling, though it was approximately offset by the condensation and nucleation of cloud droplets that it fostered. Latent heating from riming was found to be negligible.

Although vapor deposition was the largest source of latent heat, it was too far removed from the frontal surface to contribute significantly to frontogenesis. Instead, condensation and nucleation dominated the diabatic term of the frontogenesis equation. The diabatic term as a whole was found to be of comparable magnitude to the dynamic terms at midlevels, but did not contribute to frontogenesis at the surface. On the other hand, the diabatic vertical frontogenesis

term was almost everywhere larger than the dynamic vertical terms and was the primary mechanism through which high static stability was found along the frontal surface.

The vertical and horizontal frontogenesis terms were combined in a novel way to calculate the frontal slope tendency. Dynamic processes were found to increase the slope near the surface. However, the latent heating processes tended to reduce the slope of the front below 2km, especially at the surface and upwind of the front where the dynamic slope tendency term was positive. Therefore, although latent heating did contribute to horizontal frontogenesis, the primary impact of latent heating was to counteract the dynamics and weaken the front through a reduction in the frontal slope. This may at first seem to contradict other studies that find storm strengthening in the presence of strong latent heating (Montgomery and Farrell, 1991; Posselt and Martin, 2004; Čampa and Wernli, 2012; et al.). However, the pathways for strengthening often include the modification of potential vorticity and the dynamic fields. These studies address the total impact of latent heating, whereas this study only addresses the direct impact of latent heating on the isentropic structure of the warm front. Therefore our results are not inconsistent but rather add to the complete understanding of the effects of latent heating on warm fronts.

IV. Concluding Remarks

4.1. Main Conclusions

In this thesis I have presented two studies that further our understanding of warm frontal processes. In both studies, high resolution (3km horizontal grid spacing) simulations of a springtime extratropical cyclone were used to study individual cloud processes in the warm frontal zone, a topic that has not received much attention in the literature. In chapter II, budgets of total ice, cloud liquid, and rain mass were calculated whereas in chapter III a latent heating budget was presented. Vapor deposition and riming were seen to contribute about equally to the total ice mass. Likewise, condensation and nucleation both contributed significantly to cloud liquid water mass. Melting of ice particles accounted for ~75% of the production of rain, whereas warm rain collision-coalescence only accounted for ~25%. Of the processes mentioned here, only collision-coalescence does not also contribute to latent heating. Riming, being associated with the latent heat of freezing, did not contribute significantly to the latent heating budget. However, local melting rates were much higher than local riming rates, causing a strong sink of latent heat directly below the freezing level. Vapor deposition onto ice, as in the mass budget of ice, was significant in the latent heating budget above 5km; however, it was far from the warm frontal surface itself. Along the warm frontal surface, condensation and nucleation of cloud liquid water were the two largest sources of latent heat, although the melting below the freezing level reduced the net latent heating. Evaporation of rain near the surface was also strong causing additional latent cooling.

In chapter II, the sensitivity of warm frontal cloud processes to variations in cloud-nucleating aerosol concentration was tested by simulating the extratropical cyclone with three different profiles of aerosol concentration; these were representative of clean, average, and

polluted conditions. As expected, cloud droplet number concentration increased and cloud droplet size decreased with increasing pollution levels, resulting in a decreased riming efficiency. In addition there was a net decrease in the conversion of vapor to cloud liquid water (nucleation and condensation), especially in the mixed-phase region with increasing aerosol concentrations; as a result, more vapor was available for deposition onto ice species leading to an increase in that process. The increase in vapor deposition was approximately equal in magnitude to the decrease in riming, causing only a small change in the mass of ice associated with the warm front in the more polluted simulations. Melting rates were then also fairly constant across the three simulations. The conversion of cloud water to rain through collision-coalescence was also relatively insensitive to the changes in aerosol concentrations, though the reasons for this were less clear. Nonetheless, with the two rain-producing processes, melting and collision-coalescence, nearly constant, there was only a 2% increase in precipitation in the most polluted simulation over the cleanest simulation. The responses in cloud processes therefore buffer the response of precipitation to perturbations in aerosol concentration.

Differences in latent heating across the three simulations were also small. Within the mixed phase region where changes in cloud processes were largest, increases in latent heat release by vapor deposition onto ice were approximately canceled by decreases in latent heat release by riming and the conversion of vapor to cloud liquid water. As a result, vertical velocities were similar in the average across the three simulations. While this result does not reveal anything about the role of latent heating in frontal zones, it does show that aerosols, which have many potential implications for climate change, do not greatly affect the dynamics of warm fronts.

In chapter III the roles of latent heating and specific cloud processes in warm frontogenesis were explored. Condensation and nucleation of cloud water dominated the diabatic term along the frontal surface in both the horizontal and vertical components of the frontogenesis equation. Frontolysis due to melting was often collocated with the condensation and nucleation and decreased the magnitude of the diabatic terms in these locations. Frontolysis in the vertical due to rain evaporation near the surface was also strong; in the horizontal it reinforced frontogenesis due to condensation and nucleation along the frontal surface, but was frontolytic further to the north. The full diabatic term in the vertical dominated the vertical dynamic term in the frontogenesis equation almost everywhere, leading to increases in vertical stability along the frontal surface. This highlights the importance of vertical variations in cloud processes. This strong tendency of the latent heating processes to increase the vertical stability resulted in decreases of the slope of the warm front, despite the horizontal frontogenesis that the latent heating was also inducing. This result arose from the derivation and application of a new slope tendency equation. Decreases in the warm frontal slope should weaken the ability of dry dynamics to induce rising motion over the frontal surface; this is an implication of latent heating in frontal zones that has not been discussed previously.

4.2. Future Work

It was shown in these chapters that understanding the contributions of each process to these budgets can help to explain the observed precipitation distributions and dynamics associated with warm fronts. There are a number of ways in which the work presented here could be extended. First, additional warm fronts need to be examined to understand how the mass and latent heating budgets vary from storm to storm and in different environments. The case study examined here was a springtime storm, but for example, winter storms, which may

have weak or nonexistent warm rain processes, may have very different budgets of mass and latent heating. A better knowledge of the budgets may help to better understand the observed variability in warm frontal structure and precipitation. Similarly, it is not known from the one case examined how the frontogenesis due to latent heating will change in different environments. Furthermore, the implications of latent heating causing a decreased frontal slope have not been explored, but may include modifications of the precipitation distribution and frontal propagation speed, and should be explored in future work. In terms of aerosols, work should be done looking at the impact of variations in ice nuclei concentrations on warm fronts, since these could cause very different responses than were seen in the study here that only looked at variations in cloud condensation nuclei concentrations. Additionally, aerosols, whether acting as cloud condensation nuclei or ice nuclei, can cause changes in the cloud microphysical structure that could potentially be important for radiation budget of warm fronts and their parent extratropical cyclones and should also be investigated in the future. Finally, the analyses done in these studies and the suggestions for future work should also be applied to the study of cold fronts.

V. References

Ahmadi-Givi, F., G. C. Graig, and R. S. Plant, 2004: The dynamics of a midlatitude cyclone with very strong latent-heat release. *Quart. J. Roy. Meteor. Soc.*, **130**, 295-323, doi:10.1256/qj.02.226.

Albrecht, B. A., 1989: Aerosols, cloud microphysics, and fractional cloudiness. *Science*, **245**, 1227-1230.

Andreae, M. O., 2009: Correlation between cloud condensation nuclei concentration and aerosol optical thickness in remote and polluted regions. *Atmos. Chem. Phys.*, **9**, 543-556.

Baldwin, D., E.-Y. Hsie, and R. A. Anthes, 1984: Diagnostic studies of a two-dimensional simulation of frontogenesis in a moist atmosphere. *J. Atmos. Sci.*, **41**, 2686-2700.

Bannon, P. R., 1984: Effects of stratification on surface frontogenesis: warm and cold fronts. *J. Atmos. Sci.*, **41**, 2021-2026.

Baxter, M. A., P. N. Schumacher, and J. M. Boustead, 2011: The use of potential vorticity inversion to evaluate the effect of precipitation on downstream mesoscale processes. *Quart. J. Roy. Meteor. Soc.*, **137**, 179-198.

Bjerknes, J., 1919: On the structure of moving cyclones. *Geofys. Publ.*, **1**, No. 2, 1-8.
(or Bjerknes, J., 1919: On the structure of moving cyclones. *Mon. Wea. Rev.*, **47**, 95-99.)

------ and H. Solberg, 1922: Life cycle of cyclones and the polar front theory of atmospheric circulation. *Geofys. Publ.*, **3**, No. 1, 1-18.

Blier, W. and R. M. Wakimoto, 1995: Observations of the early evolution of an explosive oceanic cyclone during ERICA IOP5. Part I: Synoptic overview and mesoscale frontal structure. *Mon. Wea. Rev.*, **123**, 1288-1310.

Browning, K. A., and N. M. Roberts, 1994: Structure of a frontal cyclone. *Quart. J. Roy. Meteor. Soc.*, **120**, 1535-1557.

Čampa, J. and H. Wernli, 2012: A PV perspective on the vertical structure of mature midlatitude cyclones in the Northern Hemisphere. *J. Atmos. Sci.*, **69**, 725-740, doi:10.1175/JAS-D-11-050.1.

Carlson, T. N., 1980: Airflow through midlatitude cyclones and the comma cloud pattern. *Mon Wea. Rev.*, **108**, 1498-1509.

Catto, J. L., C. Jakob, G. Berry, and N. Nicholls, 2012: Relating global precipitation to atmospheric fronts. *Geophys. Res. Lett.*, **39**, L10805, doi:10.1029/2012GL051736.

Chan, D. and H.-R. Cho, 1991: The dynamics of moist frontogenesis in a semi-geostrophic model. *Atmos.-Ocean*, **29**, 85-101.

Clough, S. A., H. W. Lean, N. M. Roberts, and R. M. Forbes, 2000: Dynamical effects of ice sublimation in a frontal wave. *Quart. J. Roy. Meteor. Soc.*, **126**, 2405-2434.

Cotton, W. R., and Coauthors, 2003: RAMS 2001: Current status and future directions. *Meteor. Atmos. Phys.*, **82**, 5-29.

Davies, H. C., 1994: Theories of frontogenesis. *The Life Cycles of Extratropical Cyclones.* S. Gronas and M. A. Shapiro, Eds., **1**, University of Bergen, 182-192.

Davis, C. A., M. T. Stoelinga, and Y.-H. Kuo, 1993: The integrated effect of condensation in numerical simulations of extratropical cyclogenesis. *Mon. Wea. Rev.*, **121**, 2309-2330.

Eliassen, A., 1962: On the vertical circulation in frontal zones. *Geofys. Publ.*, **24**, 147-160.
Fan, J., T. Yuan, J. M. Comstock, S. Ghan, A. Khain, L. R. Leung, Z. Li, V. J. Martins, and M. Ovchinnikov, 2009: Dominant role by vertical wind shear in regulating aerosol effects on deep convective clouds. *J. Geophys. Res.*, **114**, D22206, doi:10.1029/2009JD012352.

Gedzelman, S. D. and R. Arnold, 1993: The form of cyclonic precipitation and its thermal impact. *Mon. Wea. Rev.*, **121**, 1957-1978.

Givati, A. and D. Rosenfeld, 2004: Quantifying precipitation suppression due to air pollution. *J. Appl. Meteor.*, **43**, 1038-1056.

Grams, C. M., H. Wernli, M. Böttcher, J. Čampa, U. Corsmeier, S. C. Jones, J. H. Keller, C.-J. Lenz, and L. Wiegand, 2011: The key role of diabatic processes in modifying the upper-tropospheric wave guide: a North Atlantic case-study. *Quart. J. Roy. Meteor. Soc.*, **137**, 2174-2193, doi:10.1002/qj.891.

Han, M., R. M. Rauber, M. K. Ramamurthy, B. F. Jewett, and J. A. Grim, 2007: Mesoscale dynamics of the trowal and warm-frontal regions of two continental winter cyclones. *Mon. Wea. Rev.*, **135**, 1647-1670.

Hanesiak, J. M., R. E. Stewart, K. K. Szeto, D. R. Hudak, and H. G. Leighton, 1997: The structure, water budget, and radiational features of a high-latitude warm front. *J. Atmos. Sci.*, 54, 1553-1573.

Harrington, J. Y., 1997: The effects of radiative and microphysical processes on simulation warm and transition season Arctic stratus. Ph.D. dissertation, Colorado State University, 289 pp. [Available from Department of Atmospheric Science, Colorado State University, Fort Collins, CO 80523.]

Harrold, T. W., 1973: Mechanisms influencing the distribution of precipitation within baroclinic disturbances. *Quart. J. Roy. Meteor. Soc.*, **99**, 232-251.

Haynes, J. M., R. T. Marchand, Z. Luo, A. Bodas-Salcedo, and G. L. Stephens, 2007: A multi-purpose radar simulation package: Quick-Beam. *Bull. Amer. Meteor. Soc.*, **88**, 1723-1727.

Herzegh, P. H. and P. V. Hobbs, 1980: The mesoscale and microscale structure and organization of clouds and precipitation in midlatitude cyclones. II: Warm-frontal clouds. *J. Atmos. Sci.*, **37**, 597-611.

Hewson, T. D., 1998: Objective fronts. *Meteorol. Appl.*, **5**, 37-65.

Hill, G. E., 1974: Factors controlling the size and spacing of cumulus clouds as revealed by numerical experiments. *J. Atmos. Sci.*, **50**, 3909-3927.

Hines, K. M., C. R. Mechoso, 1993: Influence of surface drag on the evolution of fronts. *Mon. Wea. Rev.*, **121**, 1152-1175.

Hobbs, P. V., 1978: Organization and structure of clouds and precipitation on the mesoscale and microscale in cyclonic storms. *Rev. Geophys. Space Phys.*, **16**, 741-755.

Hobbs, P. V., and J. D. Locatelli, 1978: Rainbands, precipitation cores and generating cells in a cyclonic storm. *J. Atmos. Sci.*, **32**, 809-819.

Hogan, R. J., P. R. Field, A. J. Illingworth, R. J. Cotton, and T. W. Choularton, 2002: Properties of embedded convection in warm-frontal mixed-phase cloud from aircraft and polarimetric radar. *Quart. J. Roy. Meteor. Soc.*, **128**, 451-476.

Houze, R. A., Jr., P. V. Hobbs, K. R. Biswas, and W. M. Davis, 1976: Mesoscale rainbands in extratropical cyclones. *Mon. Wea. Rev.*, **104**, 868-878.

Houze, R. A., Jr., S. A. Rutledge, T. J. Matejka, and P. V. Hobbs, 1981: The mesoscale and microscale structure and organization of clouds and precipitation in midlatitude cyclones. III: Air motions and precipitation growth in a warm-frontal rainband. *J. Atmos. Sci.*, **38**, 639-649.

Hsie, E.-Y., R. A. Anthes, D. Keyser, 1984: Numerical simulation of frontogenesis in a moist atmosphere. *J. Atmos. Sci.*, **41**, 2581-2594.

Huang, H.-C. and K. A. Emanuel, 1991: The effects of evaporation on frontal circulations. *J. Atmos. Sci.*, **48**, 619-628.

Hudak, D. R., R. E. Stewart, A. D. Thomson, and R. List, 1996: Warm frontal structure in association with a rapidly deepening extratropical cyclone. *Atmos.-Ocean*, **34**, 103-132.

Igel, A. L., S. C. van den Heever, C. M. Naud, S. M. Saleeby, and D. J. Posselt, 2012: Sensitivity of warm frontal processes to cloud-nucleating aerosol concentrations. In review at *J. Atmos. Sci.*

IPCC, 2007. Climate Change 2007: The Physical Science Basis. Contribution of Working Group I to the Fourth Assessment. Report of the Intergovernmental Panel on Climate Change. Ed. S. Solomon, D. Qin, M. Manning, Z. Chen, M. Marquis, K. B. Averyt, M. Tignor and H. L. Miller (Cambridge: Cambridge University Press) p 996.

Jirak, I. L., and W. R. Cotton, 2005: Effect of air pollution on precipitation along the Front Range of the Rocky Mountains. *J. Appl. Meteor. Climatol.*, **45**, 236-245.

Joos, H. and H. Wernli, 2011: Influence of microphysical processes on the potential vorticity development in a warm conveyor belt: a case-study with the limited-area model COSMO. *Quart. J. Roy. Meteor. Soc.,* **138**, 407-418, doi:10.1002/qj.934.

Kemppi, M. L. and V. A. Sinclair, 2011: Structure of a warm front: Helsinki testbed observations and model simulation. *Mon. Wea. Rev.*, **139**, 2876-2900, doi:10.1175/MWR-D-10-05003.1.

Keyser, D. and M. J. Pecnick, 1985: A two-dimensional primitive equation model of frontogenesis forced by confluence and horizontal shear. *J. Atmos. Sci.*, **42**, 1259-1282.

Khain, A. P., 2009: Notes on state-of-the-art investigations of aerosol effects on precipitation: a critical review. *Environ. Res. Lett.*, **4**, 1-20, doi:10.1088/1748-9326/4/1/015004.

Knight, D. J., and P. V. Hobbs, 1988: The mesoscale and microscale structure and organization of clouds and precipitation in midlatitude cyclones. Part XV: A numerical modeling study of frontogenesis and cold-frontal rainbands. *J. Atmos. Sci.,* **45,** 915–930.

Kuo, J. L., 1974: Further studies of the parameterization of the influence of cumulus convection on large-scale flow. *J. Atmos. Sci.*, **31**, 1232-1240.

Lilly, D. K., 1962: On the numerical simulation of buoyant convection. *Tellus*, **14**, 148-172.

Locatelli, J. D., and P. V. Hobbs, 1987: The mesoscale and microscale structure and organization of clouds and precipitation in midlatitude cyclones. XIII: Structure of a warm front. *J. Atmos. Sci*. **44**, 2290-2309.

Lynn, B., A. Khain, D. Rosefeld, and W. L. Woodley, 2007: Effects of aerosols on precipitation from orographic clouds. *J. Geophys. Res.*, **112**, D10225, doi:10.1029/2006JD007537.

Mak, M., and P. R. Bannon, 1984: Frontogenesis in a moist semi-geostrophic model. *J. Atmos. Sci*., **41**, 3485-3500.

Martin, J. E., 1998: The structure and evolution of a continental winter cyclone. Part II: Frontal forcing of an extreme snow event. *Mon. Wea. Rev.*, **126**, 329-348.

Mass, C. F. and D. M. Schultz, 1993: The structure and evolution of a simulated midlatitude cyclone over land. *Mon. Wea. Rev.*, **121**, 889-917.

Matsui, T., H. Masunaga, S. M. Kreidenweis, R. A. Pielke Sr., W.-K. Tao, M. Chin, and Y. J. Kaufman, 2006: Satellite-based assessment of marine low cloud variability associated with aerosol, atmospheric stability, and the diurnal cycle. *J. Geophys. Res.*, **111**, D17204, doi:10.1029/2005JD006097.

Miller, J. E., 1948: On the concept of frontogenesis. *J. Meteorol.*, **5**, 169-171.

Molinari, J., 1985: A general form of Kuo's cumulus parameterization. *Mon. Wea. Rev.*, **113**, 1411-1416.

Montgomery, M. T., and B. F. Farrell, 1991: Moist surface frontogenesis associated with interior potential vorticity anomalies in a semigeostrophic model. *J. Atmos. Sci.*, **48,** 343–367.

Muhlbauer, A., T. Hashino, L. Xue, A. Teller, U. Lohmann, R. M. Rasmussen, I. Geresdi, and Z. Pan, 2010: Intercomparison of aerosol-cloud-precipitation interactions in stratiform orographic mixed-phase clouds. *Atmos. Chem. Phys.*, **10**, 8173-8196, doi:10.5194/acp-10-8173-2010.

Naud, C. M. A. D. Del Genio, M. Bauer, and W. Kovari, 2010: Vertical distribution across warm and cold fronts in CloudSat-CALIPSO data and a general circulation model. *J. Climate*, **23**, 3397-3415, doi:10.1175/2010JCLI3282.1.

------, D. J. Posselt, and S. C. van den Heever, 2012: Observational analysis of cloud and precipitation in midlatitude cyclones: northern versus southern hemisphere warm fronts. *J. Climate*, in press.

Neiman, P. J., M. A. Shapiro, and L. S. Fedor, 1993: The life cycle of an extratropical marine cyclone. Part II: Mesoscale structure and diagnostics. *Mon. Wea. Rev.*, **121**, 2177-2199.

Novak, D. R., B. A. Colle, and R. McTaggart-Cowan, 2009: The role of moist processes in the formation and evolution of mesoscale snowbands within the comma head of northeast U.S. cyclones. *Mon. Wea. Rev.*, **137**, 2662-2686.

Parker, D. J. and A. J. Thorpe, 1995: The role of snow sublimation in frontogenesis. *Quart. J. Roy. Meteor. Soc.*, **121**, 763-782.

Petterssen, S., 1936: Contribution to the theory of frontogenesis. *Geofys. Publ.*, **11**, No. 6, 1-27.

Pielke, R. A., Sr., and Coauthors, 1992: A comprehensive meteorological modeling system – RAMS. *Meteor. Atmos. Phys.*, **49**, 69-91.

Pomroy, H. R. and A. J. Thorpe, 2000: The evolution and dynamical role of reduced upper-tropospheric potential vorticity in Intensive Observing Period One of FASTEX. *Mon. Wea. Rev.*, **128**, 1817-1834.

Posselt, D. J., G. L. Stephens, and M. Miller, 2008: CloudSat: Adding a new dimension to a classical view of extratropical cyclones. *Bull. Amer. Meteor. Soc.*, **89**, 599-609.

Posselt, D. J. and J. E. Martin, 2004: The effect of latent heat release on the evolution of a warm occluded thermal structure. *Mon. Wea. Rev.*, **132**, 578-599.

Ramanathan, V., R. D. Cess, E. F. Harrison, P. Minnis, B. R. Barkstrom, E. Ahmand, and D. Hartmann, 1989: Cloud-radiative forcing and climate: results from the Earth Radiation Budget Experiment. *Sci.*, **243**, 57-63.

Reeves, H. D., and G. M. Lackmann, 2004: An investigation of the influence of latent heat release on cold-frontal motion. *Mon. Wea. Rev.*, **132**, 2864-2881.

Riordan, A. J., 1990: Examination of the mesoscale features of the GALE coastal front of 24-25 January 1986. *Mon. Wea. Rev.*, **118**, 258-282.

Rutledge, S. A., P. V. Hobbs, 1983: The mesoscale and microscale structure and organizations of clouds and precipitation in midlatitude cyclones. VIII: A model for the "seeder-feeder" process in warm-frontal rainbands. *J. Atmos.Sci.*, **40**, 1185-1206.

Saleeby, S. M., W. Berg, S. van den Heever, and T. L'Ecuyer, 2010: Impact of cloud-nucleating aerosols in cloud-resolving model simulations of warm-rain precipitation in the East China Sea. *J. Atmos. Sci.*, **67**, 3916-3930.

------ and W. R. Cotton, 2004: A large-droplet mode and prognostic number concentration of cloud droplets in the Colorado State University Regional Atmospheric Modeling System (RAMS). Part I: Module descriptions and supercell test simulations. *J. Appl. Meteor.*, **43**, 182-195.

------ and ------, 2007: A binned approach to cloud-droplet riming implemented in a bulk microphysics model. *J. Appl. Meteor. and Climatol.*, **47**, 694-703, doi: 10.1175/2007JAMC1664.1.

------ and ------, D. Lowenthal, R. D. Borys, and M. A. Wetzel, 2009: Influence of cloud condensation nuclei on orographic snowfall. *J. Appl. Meteor Climatol.*, **48**, 903-922, doi:10.1175/2008JAMC1989.1.

Sawyer, J. S., 1956: The vertical circulation at meteorological fronts and its relation to frontogenesis. *Proc. Roy. Soc. London*, **234A**, 346-362.

Schneider, T., K. L. Smith, P. A. O'Gorman, and C. C. Walker, 2006: A climatology of tropospheric zonal-mean water vapor fields and fluxes in isentropic coordinates. *J. Climate*, **19**, 5918-5933.

Schultz, D. M., D. Keyser, and L. F. Bosart, 1998: The effect of large-scale flow on low-level frontal structure and evolution in midlatitude cyclones. *Mon. Wea. Rev.*, **126**, 1767-1791.

Seifert, A., C. Köhler, and K. D. Beheng, 2012: Aerosol-cloud-precipitation effects over Germany as simulated by a convective-scale numerical weather prediction model. *Atmos. Chem. Phys.*, **12**, 709-725, doi:10.5194/acp-12-709-2012.

Shapiro, M. A., and D. Keyser, 1990: Fronts, jet streams, and the tropopause. *Extratropical Cyclones, The Erik Palmén Memorial Volume,* C. W. Newton and E. Holopainen, Eds., Amer. Meteor. Soc., 167-191.

Smagorinsky, J., 1963: General circulation experiments with the primitive equations. I. The basic experiment. *Mon. Wea. Rev.*, **91**, 99-164.

Stephens G. L., D. G. Vane, R. J. Boain, G. G. Mace, K. Sassen, Z. Wang, A. J. Illingworth, E. J. O'Connor, W. B. Rossow, S. L. Durden, S. D. Miller, R. T. Austin, A. Benedetti, C. Mitrescu, and the CloudSat Science Team, 2002: The CloudSat mission and the A-TRAIN: A new dimension to space-based observations of clouds and precipitation. *Bull. Am. Meteorol. Soc*., **83**, 1771-1790.

Stevens, B. and G. Feinfold, 2009: Untangling aerosol effects on clouds and precipitation in a buffered system. *Nature*, **461**, 607-613, doi:10.1038/nature08281.

Stewart, R. E., K. K. Szeto, R. F. Reinking, S. A. Clough, and S. P. Ballard, 1998: Midlatitude cyclonic cloud systems and their features affecting large scales and climate. *Rev. Geophys.*, **36**, 245-273.

Stoelinga, M. T., 1996: A potential vorticity-based study of the role of diabatic heating and friction in a numerically simulated baroclinic cyclone. *Mon. Wea. Rev.*, **124**, 849-874.

Storer, R. L., S. C. van den Heever, and G. L. Stephens, 2010: Modeling aerosol impacts on convective storms in different environments. *J. Atmos. Sci.*, **67**, 3904-3915, doi:10.1175/2010JAS3363.1.

Szeto, K. K., and R. E. Stewart, 1997: Effects of melting on frontogenesis. *J. Atmos. Sci.*, **54**, 689-702.

Tao, W.-K., J-P. Chen, Z. Li, C. Wang, and C. Zhang, 2012: Impact of aerosols on convective clouds and precipitation. *Rev. Geophys.*, **50**, RG2001, doi:10.1029/2011RG000369.

Thorpe, A. J. and K. A. Emanuel, 1985: Frontogenesis in the presence of small stability to slantwise convection. *J. Atmos. Sci.*, **42**, 1810-1824.

Trenberth, K. E. and D. P. Stepaniak, 2003: Covariability of components of poleward atmospheric energy transports of seasonal and interannual timescales. *J. Climate,* **16**, 3691-3705.

Twomey, S., 1977: The influence of pollution on the shortwave albedo of clouds. *J. Atmos. Sci.*, **34**, 1149-1152.

van den Heever, S. C., G. L. Stephens, and N. B. Wood, 2011: Aerosol indirect effects on tropical convection characteristics under conditions of radiative-convective equilibrium. *J. Atmos. Sci.*, **68**, 699-718.

Wakimoto, R. M., W. Blier, and C. Liu, 1992: The frontal structure of an explosive oceanic cyclone: Airborne radar observations of ERICA IOP4. *Mon. Wea. Rev.*, **120**, 1135-1155.

Wakimoto, R. M. N. T. Atkins, and C. Liu, 1995: Observations of the early evolution of an explosive oceanic cyclone during ERICA IOP 5. Part II: Airborne Doppler analysis of the mesoscale circulation and frontal structure. *Mon. Wea. Rev.*, **123**, 1311-1327.

Wang, J., S. C. van den Heever, and J. S. Reid, 2009: A conceptual model for the link between Central American biomass burning aerosols and severe weather over the south central United States. *Environ. Res. Lett.*, **4**, 1-9, doi:10.1088/1748-9326/4/1/015003.

Whitaker, J. S., and C. A. Davis, 1994: Cyclogenesis in a saturated environment. *J. Atmos. Sci.*, **51**, 889-907.

Woods, C. P., J. D. Locatelli, and M. T. Stoelinga, 2007: The IMPROVE-1 Storm of 1-2 February 2001. Part IV: precipitation enhancement across the melting layer. *J. Atmos. Sci.*, **65**, 1087-1992, doi: 10.1175/2007JAS2247.1.

Xue, H. and G. Feingold, 2005: Large-eddy simulations of trade wind cumuli: Investigation of aerosol indirect effects. *J. Atmos. Sci.*, **63**, 1605-1622.